

# Loading and Co-Solvent-Triggered Release of Okanin, a C<sub>4</sub> Plant Key Enzyme Inhibitor, into/from Functional Microgels

Jonas Dittrich<sup>a,b,†</sup>, Fabian Kolodzy<sup>a,c,d,†</sup>, Alexander Töpel<sup>a,c,d</sup>, Alexander Hofmann<sup>a,e</sup>,  
Georg Groth<sup>a,e</sup>, Andrij Pich<sup>\*,a,c,d,f</sup>, Holger Gohlke<sup>\*,a,b,g</sup>

<sup>†</sup>These authors contributed equally.

<sup>a</sup>Bioeconomy Science Center (BioSC), Forschungszentrum Jülich, 52425 Jülich, Germany

<sup>b</sup>Institute for Pharmaceutical and Medicinal Chemistry, Heinrich Heine University Düsseldorf, 40225 Düsseldorf, Germany

<sup>c</sup>DWI-Leibniz-Institute for Interactive Materials, RWTH Aachen University, 52056 Aachen, Germany

<sup>d</sup>Institute of Technical and Macromolecular Chemistry, RWTH Aachen University, 52074 Aachen, Germany

<sup>e</sup>Institute of Biochemical Plant Physiology, Heinrich Heine University Düsseldorf, 40225 Düsseldorf, Germany

<sup>f</sup>Aachen Maastricht Institute for Biobased Materials, Maastricht University, Geleen, 6167 RD Netherlands

<sup>g</sup>John von Neumann Institute for Computing (NIC), Jülich Supercomputing Centre (JSC), and Institute of Bio- and Geosciences (IBG-4: Bioinformatics), Forschungszentrum Jülich GmbH, 52425 Jülich, Germany

Keywords: microgel carrier, all-atom molecular dynamics simulations, herbicide, free energy

Author ORCID:

Jonas Dittrich: 0000-0003-2377-2268

Fabian Kolodzy: 0000-0002-0311-0913

Alexander Töpel: 0000-0002-6801-2222

Alexander Hofmann: 0000-0001-8417-6748

Georg Groth: 0000-0002-1806-9861

Andrij Pich: 0000-0003-1825-7798

Holger Gohlke: 0000-0001-8613-1447

\*Corresponding Authors:

Andrij Pich

Address: Forckenbeckstr. 50, 52056 Aachen, Germany.

Phone: (+49) 241 80 23310

E-mail: pich@dwirwth-aachen.de

Holger Gohlke

Address: Universitätsstr. 1, 40225 Düsseldorf, Germany.

Phone: (+49) 211 81 13662; Fax: (+49) 211 81 13847

E-mail: gohlke@uni-duesseldorf.de

# 1 Abstract

2 The constantly growing world population leads to increasing demands for food, which  
3 challenges modern agriculture manifold. Pests, such as weeds, require the application of  
4 agrochemicals to increase crop yield. Due to the environmental impact of these potentially  
5 hazardous chemicals, the demand for more efficient formulations is increasing. Promising  
6 formulations consist of easily adaptable carriers from which controllable stimuli release the  
7 agrochemicals. Here, we investigated poly(*N*-vinylcaprolactam) (pVCL)-based microgels as a  
8 potential carrier for okanin, an inhibitor of the C<sub>4</sub> plant key enzyme phosphoenolpyruvate  
9 carboxylase, by combining experiments, molecular simulations, and free energy computations.  
10 Dynamic light scattering, scanning transmission electron and atomic force microscopy revealed  
11 that pVCL microgels collapse and rigidify upon the loading of okanin. The simulations identified  
12 loosely adsorbed okanin and tightly bound okanin mediating inter-chain crosslinks. With  
13 increasing okanin concentration, stacking interactions of okanin occur with adsorbed and bound  
14 okanin. These findings can explain the experimentally observed collapse and the rigidification of  
15 the microgels. Based on the atomistic insights, two poly(*N*-vinylcaprolactam-*co*-glycidyl  
16 methacrylate) microgels were synthesized, for which a doubled loading capacity of okanin was  
17 found. Finally, we investigated the triggered release of okanin using the addition of green solvents  
18 as a stimulus both *in vitro* and *in planta*. This work establishes a basis for the further optimization  
19 of pVCL-based microgels as a carrier for the delivery of polyphenolic agrochemicals.

## 21    **2 Introduction**

22        Sustainable agriculture is of vital importance considering the growing world population. Crop  
23    productivity can be significantly increased by the use of fertilizers and pesticides.<sup>1</sup> However, wash  
24    off by rain, or spray drifts of the applied agrochemicals lead to a reduction of the applied amount  
25    of active ingredients.<sup>2-3</sup> Consecutively, the applied chemicals accumulate in the soil and  
26    groundwater, posing serious health risks for humans and animals. Therefore, reducing the  
27    environmental impact of hazardous chemicals is one of the most important challenges of modern  
28    sustainable agriculture. It can be addressed by either replacing chemicals with ecologically  
29    friendly alternatives or their encapsulation to ensure a long-term release or release-on-demand  
30    mechanism triggered by a specific stimulus.<sup>4-5</sup>

31        Different pathogens and pests are estimated to yield losses of up to 40%.<sup>6</sup> Without adequate  
32    protection, losses potentially rise to 80%.<sup>7</sup> Among all pests, weeds are possibly responsible for the  
33    highest loss.<sup>7</sup> Weeds are a major threat to global food production due to a rapid formation of  
34    resistance against commonly used herbicides. Hence, the constant development of novel  
35    herbicides is necessary. Chalcones are promising lead structures for the development of C<sub>4</sub> plant  
36    selective herbicides.<sup>8-10</sup> The natural polyphenolic compound okanin (2',3',4',3,4-Pentahydroxy-  
37    chalcone) was shown to be an efficient inhibitor of phosphoenolpyruvate carboxylase, a key  
38    enzyme for carbon fixation and biomass increase in the C<sub>4</sub> photosynthetic pathway of many of the  
39    world's most damaging weeds.<sup>8, 11</sup>

40        Microgels are crosslinked, macromolecular, porous colloids, usually showing high softness  
41    and deformability. In solution, many common microgels form stable dispersions and show a  
42    stimuli-responsive swelling.<sup>12-13</sup> The stimuli-responsiveness can be exploited for the controlled  
43    uptake and release of different substances by using triggers such as temperature<sup>14-15</sup>, pH<sup>16</sup>, and  
44    different solvents. A targeted release can be achieved by tailoring the responsiveness to these  
45    triggers. Recently, microgels have attracted attention as a versatile carrier and release system for  
46    metal ions<sup>17</sup>, small molecules<sup>14, 18-21</sup>, biomacromolecules<sup>22-24</sup>, and even cells<sup>25</sup>. Many common  
47    monomers such as *N*-vinylcaprolactam (VCL) are suited for biological and medical applications  
48    due to the biocompatibility of the formed microgels.<sup>26</sup> Poly(*N*-vinylcaprolactam) (pVCL) is used  
49    for tissue engineering<sup>27</sup> and drug delivery<sup>14, 18-19</sup> as the lower critical solution temperature (LCST)  
50    is close to the human body temperature (~32 °C in water).<sup>28</sup> Polymer chains can be crosslinked  
51    either by forming new covalent bonds, e.g., with bifunctional monomers such as  
52    *N,N'*-methylenebis(acrylamide) (BIS), or by exploiting strong non-covalent interactions.<sup>29-31</sup> The  
53    latter is especially suited for the synthesis of degradable microgels, e.g., microgels crosslinked  
54    with the polyphenolic tannic acid, which degrade at basic conditions due to deprotonation of the

hydroxy groups.<sup>30-31</sup> Reactive co-monomers such as glycidyl methacrylate (GMA) can be utilized for post-polymerization modification via the addition of nucleophiles to the epoxy group.<sup>32-33</sup> pVCL-based microgels with a GMA-rich shell provide access to specific surface functionalization.<sup>34</sup> For the use of microgels in plant protection, the stimuli-responsiveness enables release as needed so agrochemicals can be retained over a longer period. This results in fewer applications per harvesting season and, thus, reduced operating costs, while simultaneously reducing the ecological footprint.<sup>35-36</sup> Furthermore, microgels can be modified to increase their adhesion to leaves and improve their rain-fastness. Anchor peptides, i.e., small peptides that bind to the wax layer of the plant leaves,<sup>37</sup> were successfully used to increase the rain-fastness of pesticide formulations. Microgels functionalized with anchor peptides were successfully used for the foliar fertilization of cucumber plants with Fe<sup>3+</sup>-ions.<sup>17</sup>

pVCL interacts with polyphenolic moieties, as shown in the supramolecular crosslinking of pVCL with tannic acid by hydrogen bonds.<sup>30</sup> Thus, pVCL-based microgels should be promising candidates for binding okanin. However, a pH-triggered release of okanin from the carrier is unsuited as the resulting salt stress leads to a reduction in crop yield and quality.<sup>38-39</sup> Green solvents<sup>40-41</sup>, which are environmentally compatible and authorized as additives in agricultural applications, provide a suitable alternative.

In this work, we investigate pVCL-based microgels as a potential carrier for the C<sub>4</sub> plant key enzyme inhibitor okanin, which could lead to an aqueous formulation with increased okanin loading and/or a long-term release or a release-on-demand mechanism. In an interdisciplinary approach, we combined experiments and molecular simulations to investigate the loading of okanin into pVCL-based microgels, elucidate the binding mode, and scrutinize the co-solvent-triggered release. In more detail, we investigated the uptake of okanin into pure pVCL-based microgels under laboratory conditions using UV/Vis spectroscopy. Changes in the microgels' size upon okanin loading were traced via dynamic light scattering (DLS), and changes in the microgels' morphology were investigated using scanning transmission electron (STEM) and atomic force microscopy (AFM). Next, using all-atom molecular dynamics (MD) simulations of the uptake of okanin into the pVCL-based microgels, we obtained insights into the binding mode at the atomistic level. To improve the loading capacity of the microgel, we investigated the type of interaction between okanin and pVCL. Based on the simulation results, we incorporated glycidyl methacrylate (GMA) in both the core and shell of the pVCL microgels to increase the overall loading of okanin. Finally, we combined experimental and computational methods to analyze the co-solvent triggered release of okanin from microgels.

### 88 3 Materials and Methods

89 **Materials.** *N*-Vinylcaprolactam (VCL, TCI, > 98,0%) was distilled and recrystallized from  
90 *n*-hexane. Glycidyl methacrylate (GMA, Sigma-Aldrich, 97%) was distilled before use.  
91 2,2'-Azobis(2-methylpropionamidine) dihydrochloride (AMPA, Sigma-Aldrich, 97%),  
92 *N,N'*-methylenbis(acrylamide) (BIS, Sigma-Aldrich, 99%), acetic acid (AcOH, Sigma-Aldrich,  
93  $\geq 99.0\%$ ), dimethyl sulfoxide (DMSO, Sigma-Aldrich,  $\geq 99.0\%$ ), ethyl acetate (EtOAc, VWR  
94 Chemicals, 99.0%), and water (H<sub>2</sub>O, Merck-Millipore, LC-MS-grade) were used without further  
95 purification.

96 **UV/Vis spectroscopy.** UV/Vis spectra were measured with a Jasco V-780 UV-Visible/NIR  
97 spectrophotometer equipped with the USE-753 cuvette holder in the range of 300 nm to 800 nm  
98 in steps of 0.5 nm and a scanning speed of 400 nm min<sup>-1</sup>. Samples in an aqueous solution were  
99 measured in polystyrene cuvettes against ultra-pure water. Samples in DMSO were measured in  
100 Quartz SUPRASIL cuvettes from Hellma Analytics against DMSO. The optical path length of all  
101 cuvettes was 1.0 cm. To obtain maximum absorbance < 1.1, samples were diluted accordingly for  
102 all measurements.

103 **Dynamic light scattering.** Dynamic light scattering (DLS) was measured at 20 °C and 50 °C  
104 with a Zetasizer Nano ZS from Malvern, operating a laser at 632.8 nm with a power of 4 mW. The  
105 scattering angle was fixed to  $\Phi = 173^\circ$ . Sample dispersions were prepared in ultra-pure water and  
106 measured in polystyrene cuvettes. The concentrations of the stock solutions of unloaded microgels  
107 are described in the Supplemental Materials and Methods. For unloaded microgels, 5  $\mu$ L of the  
108 microgel stock solution were added to 1200  $\mu$ L of ultra-pure water ( $c_{\text{DLS, sample}} = \sim 50 \mu\text{g mL}^{-1}$ ). For  
109 okanin-loaded microgels ( $c_{\text{stock}} = 1 \text{ mg mL}^{-1}$ ), 36  $\mu$ L of the microgel stock solution were added to  
110 1200  $\mu$ L of ultra-pure water ( $c_{\text{DLS, sample}} = \sim 30 \mu\text{g mL}^{-1}$ ). A lower concentration for okanin-loaded  
111 microgels was chosen to account for the increased turbidity. Before each measurement, the  
112 temperature of the sample was equilibrated for 3 min. Measurements were repeated three times for  
113 each sample.

114 **Raman spectroscopy.** Raman spectra were measured on an RFS 100/s Raman spectrometer  
115 by Bruker with an Nd:YAG laser ( $\lambda = 1064 \text{ nm}$ ) with a spectral resolution of 4 cm<sup>-1</sup>, a power of  
116 200 mW, and 1000 scans in the range of 4000 cm<sup>-1</sup> to 300 cm<sup>-1</sup>. Samples were pressed into an  
117 aluminum pan before measurement. All spectra were baseline-corrected and normalized to the  
118 maximum if not stated otherwise.

119 **Atomic force microscopy.** Atomic force microscopy (AFM) was performed using a Veeco  
120 Instruments Nanoscope V microscope. An NCH POINTPROBE-Silicon SPM-sensor from  
121 NanoWorld, with a resonance frequency of 320 kHz, and a force constant of 42 N m<sup>-1</sup> was used

122 as the cantilever. Images were recorded in tapping mode and analyzed with the software  
123 Gwyddion<sup>42</sup> (v. 2.51). Before use, silicon wafers were washed with toluene, dried with nitrogen,  
124 and activated with a Flecto10USB-MFC plasma etcher (Plasma Technology) with an air plasma  
125 at 0.2 mbar and a power of 100W for 180 s. The coating was achieved by spin coating 50  $\mu$ L of  
126 the microgel dispersion (1.0 mg mL<sup>-1</sup>) on the activated wafer at 2000 rpm for 60 s with a WS-  
127 650SZ-6NPP/LITE spin coater by Laurell.

128 **Scanning transmission electron microscopy.** Scanning transmission electron microscopy  
129 (STEM) measurements were performed on an Ultra-high Resolution Scanning Electron  
130 Microscope SU9000 (Hitachi-High Technologies America, Inc.) operating at a voltage of 30 kV.  
131 Therefore, 20  $\mu$ L of a diluted microgel dispersion (0.1 g L<sup>-1</sup>) were dropped on a TEM-grid (Carbon  
132 Film 200 Mesh Copper Grids, Electron Microscopy Sciences) and dried at room temperature overnight.  
133 All samples were sputtered with 2 nm carbon before the analysis. Images were analyzed with the  
134 software ImageJ<sup>43</sup>.

135 **Microgel synthesis and characterization.** All pVCL-based microgels were synthesized by  
136 precipitation polymerization<sup>32-34</sup> with 10.538 mmol of monomers in 100 mL of ultra-pure water.  
137 The amount of VCL was 97.4 mol% (1428.6 mg, 10.264 mmol) for pure pVCL and 87.4 mol%  
138 (1282.0 mg, 9.210 mmol) for p(VCL-co-GMA). The amount of GMA in p(VCL-co-GMA) was  
139 10.0 mol% (149.8 mg, 144  $\mu$ L, 1.054 mmol, 10.0 mol%). 0.6 mol% AMPA (17.1 mg, 63  $\mu$ mol)  
140 were used as the initiator and 2.0 mol% BIS (32.5 mg, 211  $\mu$ mol) as the crosslinker. The  
141 composition of the microgels is summarized in Table S1.

142 The enrichment of GMA in the core (p(VCL/GMA<sub>core</sub>)) was achieved in a batch reaction  
143 according to Hüntzschel et al. due to the higher reactivity of GMA compared to VCL.<sup>32-33</sup> A GMA-  
144 rich shell (p(VCL/GMA<sub>shell</sub>)) was obtained using a semi-batch approach with delayed addition of  
145 GMA as done in previous studies.<sup>34</sup> The GMA content of the lyophilized microgels was  
146 determined using Raman spectroscopy following an established procedure and was determined  
147 with 9.8 mol% and 10.7 mol% for p(VCL/GMA<sub>core</sub>) and p(VCL/GMA<sub>shell</sub>), respectively.<sup>34</sup> The  
148 Raman spectra are depicted in Figure S1. The microgels' morphology was investigated by AFM  
149 and STEM. The hydrodynamic radius ( $R_H$ ) and the polydispersity index (PDI) as well as the  
150 volume phase transition temperature (VPTT) were determined by DLS. The temperature-  
151 dependent results for  $R_H$  as well as the results for the VPTT are depicted in Figure S2. More details  
152 on the microgel synthesis, the quantification of the GMA content by Raman spectroscopy, and the  
153 confirmation of the thermoresponsive properties are provided in the Supplemental Materials and  
154 Methods.

155

156       **Loading of microgels with okanin.** The okanin loading was investigated for pVCL,  
157 p(VCL/GMA<sub>shell</sub>), and p(VCL/GMA<sub>core</sub>). The workflow for the loading and purification process is  
158 depicted in Figure 1A. A microgel stock solution (13.69 mg mL<sup>-1</sup>, 17.47 mg mL<sup>-1</sup> and  
159 13.42 mg mL<sup>-1</sup> for pVCL, p(VCL/GMA<sub>core</sub>), and p(VCL/GMA<sub>shell</sub>), respectively) was used to  
160 prepare 2000 µL of a diluted microgel dispersion (1.0 mg mL<sup>-1</sup>) in 2 mL centrifuge tubes. Okanin  
161 dissolved in DMSO was added to the microgel dispersions to obtain okanin concentrations of  
162 0.014 mM, 0.05 mM, 0.1 mM, 0.5 mM, 1.0 mM, 1.3 mM, and 2.0 mM. DMSO was added so that  
163 the total volume of DMSO in each sample was 48 µL (2.4 vol.-%). For the microgels, these okanin  
164 concentrations correspond to a molar ratio  $n_{\text{okanin}}/n_{\text{CU}}$  of 0.002, 0.007, 0.014, 0.070, 0.139, 0.181,  
165 and 0.278, respectively, where  $n_{\text{okanin}}$  is the amount of okanin and  $n_{\text{CU}}$  is the number of the  
166 constitutional units (CU). The samples were mixed for 3 h. Quartz Crystal Microbalance with  
167 Dissipation monitoring (QCM-D, see Supplemental Material and Methods) experiments confirm  
168 the completion of the uptake within this time (Figure S3). Afterward, the dispersions were  
169 centrifuged for 5 min at 43 rcf (relative centrifugal force), and 1000 µL of the supernatant was  
170 taken for further purification. The microgel dispersion was centrifuged for 20 min at 6708 rcf, the  
171 supernatant was removed, and the microgel dispersion was re-dispersed in ultra-pure water. This  
172 step was repeated thrice. All loading experiments were done as triplicates.  $R_H$  and PDI of the  
173 loaded microgels were determined by DLS. Additionally, AFM and STEM were applied to  
174 determine the radius of the width ( $R_{\text{AFM}}$ ,  $R_{\text{STEM}}$ ) and the height ( $H_{\text{AFM}}$ ) of the microgels.

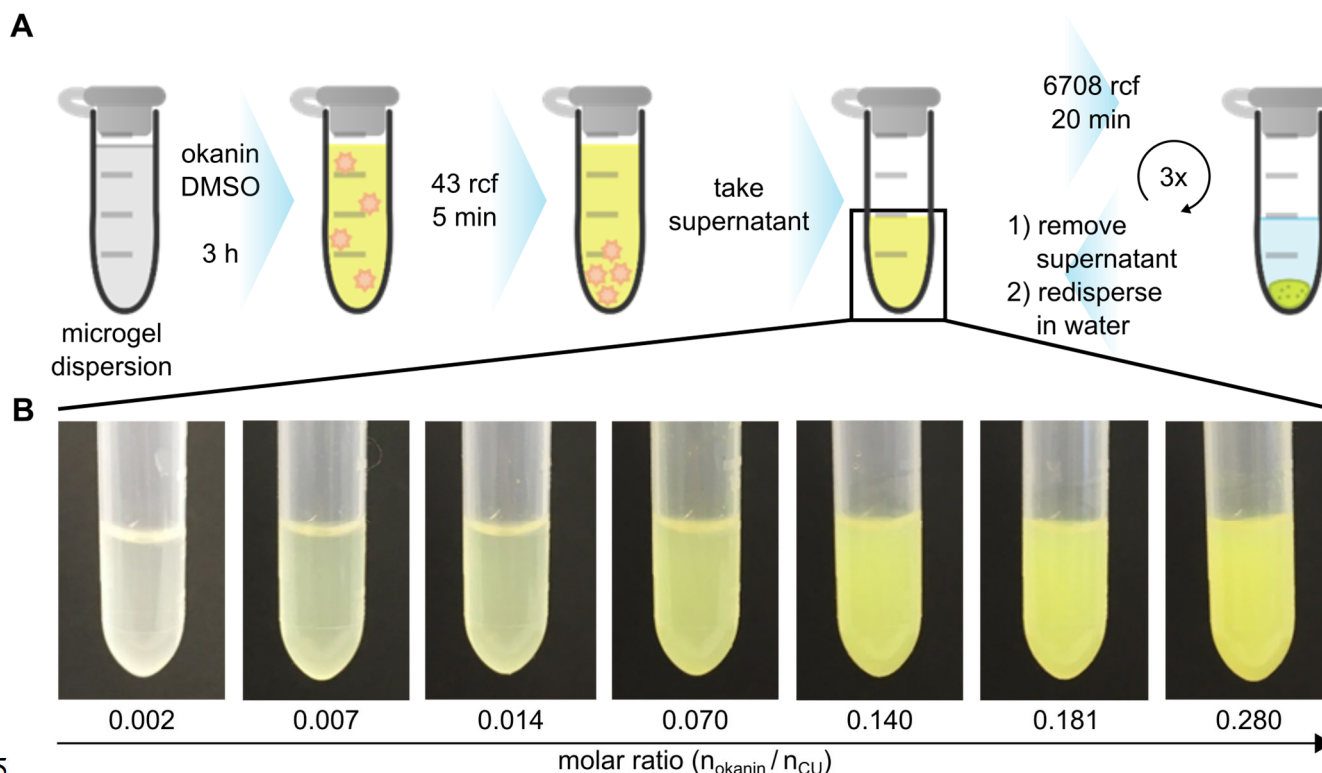


**Figure 1:** Experimental workflow and exemplary images for the loading of okanin into microgels. **A** Schematic workflow for the okanin loading and purification of the microgels. **B** Images of purified pVCL microgels loaded with varying amounts of okanin in relation to the number of constitutional units ( $n_{\text{okanin}}/n_{\text{CU}}$ ). Schematics in this figure were created with Chemix (<https://chemix.org>).

**Determination of the attenuation coefficient.** Due to the low solubility, a stock solution of okanin could not be prepared in ultra-pure water. Thus, the attenuation coefficient was determined in a 2.4 vol.-% DMSO/water solution. For the first sample, an okanin stock solution in DMSO ( $c_{\text{stock}} = 1.332 \text{ mM}$ ) was prepared and  $60 \mu\text{L}$  of the stock solution were added to  $2500 \mu\text{L}$  of ultra-pure water such that the final okanin concentration was  $31.22 \mu\text{M}$ . After measurement of the UV/Vis spectrum,  $1280 \mu\text{L}$  of the solution were diluted in  $1280 \mu\text{L}$  of a 2.4 vol.-% DMSO/water solution to obtain an okanin concentration of  $15.61 \mu\text{M}$ . This dilution series was continued for concentrations of  $7.81 \mu\text{M}$ ,  $3.92 \mu\text{M}$ ,  $1.94 \mu\text{M}$ , and  $0.97 \mu\text{M}$ . The dilution series was prepared and measured in triplicates. The UV/Vis spectra are depicted in Figure S4. The average of the maximum absorbance at  $377 \text{ nm}$  for each point was calculated (Table S2) and plotted against the okanin concentration (Figure S5). The attenuation coefficient  $\varepsilon$  is equal to the slope of the linear fit ( $\varepsilon_{377 \text{ nm}} = (3126 \pm 14) \cdot 10^1 \text{ L mol}^{-1} \text{ cm}^{-1}$ ). Analogously,  $\varepsilon$  was determined in pure DMSO as the absorption maximum exhibits a bathochromic shift ( $\varepsilon_{392 \text{ nm}} = (3279 \pm 17) \cdot 10^1 \text{ L mol}^{-1} \text{ cm}^{-1}$ ), which is also observed for the binding of okanin to the microgels (Figure S6). The corresponding UV/Vis spectra are depicted in Figure S7 and the mean values for the maximal absorbance are listed in Table S3.



196 **Measuring the loading of okanin into the microgel via UV/Vis.** The loading of okanin into  
 197 the microgels was determined by UV/Vis spectroscopy. 75  $\mu\text{L}$  of the microgel stock solution  
 198 ( $c_{\text{stock}} = 1 \text{ mg mL}^{-1}$ ) were added to 2500  $\mu\text{L}$  of ultra-pure water ( $c_{\text{sample}} = \sim 30 \text{ } \mu\text{g mL}^{-1}$ ). As the  
 199 turbidity of the solution depends on the initial okanin concentration (Figure 1B), the baseline  
 200 correction could not be performed using the baseline of dispersed unloaded microgels. Instead, we  
 201 performed a baseline correction that is independent of the swelling state of the microgel. A  
 202 comparison of different baseline correction methods revealed that an exponential baseline  
 203 correction is more suited than a linear baseline correction (Figure S8). The exponential baseline is  
 204 defined as depicted in eq. 1:

$$A = a \cdot e^{b \cdot \lambda} \quad \text{eq. 1}$$

205 where  $A$  is the absorbance at a certain wavelength,  $\lambda$  is the wavelength, and  $a$  and  $b$  are the  
 206 fitting parameters.  $a$  and  $b$  were determined for each spectrum via a two-point method for  
 207  $\lambda_1 = 300 \text{ nm}$  and  $\lambda_2 = 550 \text{ nm}$  according to eq. 2 and eq. 3, respectively.

$$b = \frac{\ln\left(\frac{A_{\lambda_1}}{A_{\lambda_2}}\right)}{\lambda_1 - \lambda_2} \quad \text{eq. 2}$$

$$a = \frac{A_{\lambda_2}}{e^{b \cdot \lambda_2}} \quad \text{eq. 3}$$

208 The fitting parameters  $a$  and  $b$  as well as the maximal absorbance  $A_{\text{max}}$  before and after  
 209 correction are listed in the Supporting Information (Table S3 for the calibration in DMSO and  
 210 Table S4-6 for the loading of okanin into a pVCL, a p(VCL/GMA<sub>core</sub>) and a p(VCL/GMA<sub>shell</sub>)  
 211 microgel, respectively). This correction was also applied to the calibration spectra (Figure S7) to  
 212 obtain the corrected attenuation coefficient  $\varepsilon_{392 \text{ nm,corr.}} = (3176 \pm 17) \cdot 10^1 \text{ L mol}^{-1} \text{ cm}^{-1}$   
 213 (Figure S5).

214 **Co-solvent-triggered release.** The co-solvent-triggered release was investigated for pVCL,  
 215 p(VCL/GMA<sub>shell</sub>), and p(VCL/GMA<sub>core</sub>) loaded at an initial okanin concentration of 0.5 mM and  
 216 1.3 mM corresponding to a molar ratio of 0.070 and 0.181, respectively. The values of initial  
 217 loading are shown in Table S7-9 for pVCL, p(VCL/GMA<sub>shell</sub>), and p(VCL/GMA<sub>core</sub>), respectively.  
 218 500  $\mu\text{L}$  of the okanin-loaded microgel dispersion ( $1.0 \text{ mg mL}^{-1}$ ) were prepared in 1.5 mL  
 219 centrifuge tubes. For water, DMSO, and AcOH, 50.0  $\mu\text{L}$  (10.0 vol.-%) of the respective co-solvent  
 220 were added. In the case of EtOAc, a mixture of 47.0  $\mu\text{L}$  of EtOAc (9.4 vol.-%) and 3.0  $\mu\text{L}$  of ultra-  
 221 pure water was added due to the low solubility of EtOAc in water. The samples were mixed for  
 222 16 h. QCM-D experiments confirm the completion of the release within this time (Figure S3).  
 223 Afterward, the dispersions were centrifuged for 20 min at 6708 rcf. 400  $\mu\text{L}$  of the supernatant were

taken and diluted with 400  $\mu\text{L}$  and 1200  $\mu\text{L}$  of ultra-pure water for samples of microgels loaded at a molar ratio of 0.181 and 0.070, respectively, to determine the amount of released okanin by UV/Vis spectroscopy. All release experiments were performed in triplicates.

**Computational approach.** pVCL microgels often show a characteristic core-shell structure due to a gradient in crosslink density within the microgel resulting in a densely crosslinked core and less crosslinked shell.<sup>44</sup> To account for this core-shell structure of our microgel, we investigated the interaction of okanin with a syndiotactic linear pVCL 50mer ( $M_w \approx 7,000 \text{ g mol}^{-1}$ ), which represents the loosely crosslinked shell, as well as with a methyl-BIS-crosslinked cubic pVCL model with an inter-crosslink chain length of 20 repeating units ( $M_w \approx 34,750 \text{ g mol}^{-1}$ ), representing the densely crosslinked core (Figure 2).

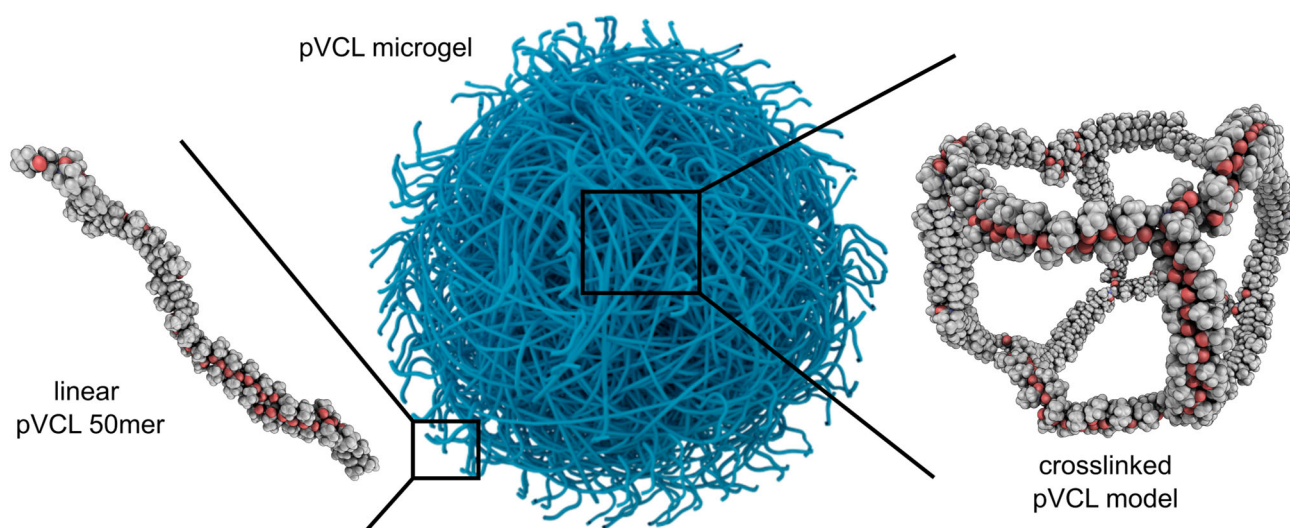


**Figure 2:** Decomposition of a microgel into atomistic models for the shell and core section. Simulations of linear oligomers mimic the loosely crosslinked shell of the microgel (left); the BIS-crosslinked cubic pVCL models mimic the highly crosslinked core (right).

We chose the representative models based on initial tests, in which we investigated the effect of the tacticity and crosslink density on the BIS-crosslinked polymers' thermo-responsiveness by simulating three different atactic as well as one syndiotactic and one isotactic polymer cube with an inter-crosslink chain length of 20 and 40 repeating units, respectively. For each tacticity, ten replicas were simulated for 500 ns at 293 K, 313 K, and 343 K in the TIP3P<sup>45</sup> water model, resulting in a cumulative simulation time of 150  $\mu\text{s}$  (Table S10). In line with previous experiments<sup>46</sup>, we found a dependency of the phase transition of the pVCL model on the polymer's tacticity. Atactic and isotactic pVCL models collapse irrespective of the temperature and inter-crosslink chain length (Figure S9 and Figure S10). Syndiotactic pVCL showed the expected thermo-responsiveness irrespective of the inter-crosslink chain length and was selected as a model representing the core section of a pVCL microgel. To evaluate the influence of the chosen water model, we performed simulations of a crosslinked pVCL model with an inter-crosslink chain

length of 20 in OPC<sup>47</sup> water (Table S11), resulting in a cumulative simulation time of 75  $\mu$ s. In agreement with previous studies,<sup>46</sup> the collapse of the syndiotactic pVCL is well-defined using TIP3P water (Figure S9 and Figure S10), whereas the collapse is less pronounced in OPC water (Figure S11).

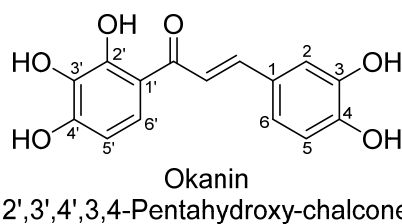
To elucidate the binding mode of the herbicide okanin with the pVCL microgel carrier at an atomistic level, we employed extensive all-atom MD simulations of systems comprising linear or crosslinked pVCL with varying concentrations of okanin. We examined the influence of the okanin concentration by increasing the number of okanin molecules, going from a simulation in pure water to a molar ratio  $n_{\text{okanin}}/n_{\text{CU}}$  of 0.04, 0.14, 0.28, 0.56 to 1.11 and 0.14, 0.56 to 1.11 for the crosslinked and the linear pVCL, respectively. An overview is provided in Table S12.

To further assess the impact of okanin at different concentrations on the polymers' conformation and thermo-responsiveness, we simulated ten replicas for 1  $\mu$ s each at 293 K and 313 K for each okanin concentration, yielding a cumulative simulation time of 60  $\mu$ s and 120  $\mu$ s for the linear and the crosslinked pVCL, respectively.

Furthermore, we investigated the effect of ethyl acetate on the pVCL cube with an inter-crosslink chain length of 20 repeating units. Ethyl acetate is considered a preferred/recommended solvent<sup>40-41</sup> and can potentially be used to promote okanin release from the microgel. However, we note that it is not commonly used in agricultural applications and, thus, serves as an organic solvent reference and a benchmark in our study. We selected the crosslinked systems with a low (0.04) and high (0.28) initial  $n_{\text{okanin}}/n_{\text{CU}}$  and simulated each for 1  $\mu$ s, yielding an additional cumulative simulation time of 80  $\mu$ s for the okanin release.

**Structure preparation.** The generation of the parameters for the pVCL repeating unit was described in detail in our previous work.<sup>46</sup> For computing atomic charges, we followed the Restrained Electrostatic Potential (RESP) procedure.<sup>48</sup> The electrostatic potential (ESP) was calculated at the HF/6-31G\* level using Gaussian09.<sup>49</sup> Afterwards, the ESP was fitted using the RESP charge fitting procedure implemented in antechamber.<sup>50</sup> We employed the same procedure for the tetra-methylated BIS moiety and okanin. The protonation state of okanin was determined using Epik<sup>51</sup> within Schrödinger's Maestro<sup>52</sup> program, revealing a predicted  $pK_a$  value of 7.3 for the hydroxy group at position 4' (Scheme 1), which we consider deprotonated in our simulations. For okanin, missing force field parameters were generated using the parmchk2 module of Amber20<sup>53</sup>. Oligomeric pVCL and the crosslinked pVCL structures were generated using the tleap module of Amber20. The library (lib) and parameter modification (frcmod) files used are available at <http://dx.doi.org/10.25838/d5p-41>. Finally, the remaining open valence of the BIS moieties within the crosslinked pVCL model and the termini of the linear pVCL oligomers were methyl-

terminated. According to DLS measurements, the radius of the (swollen) microgel models is ~100-fold smaller than that of the experimental microgels.



**Scheme 1:** Chemical structure of okanin (2',3',4',3,4-Pentahydroxy-chalcone). Okanin has been identified as a selective inhibitor of phosphoenolpyruvate carboxylase, a key enzyme for carbon fixation in the C<sub>4</sub> photosynthetic pathway of damaging weeds.<sup>8</sup>

**Molecular dynamics simulations and analysis.** MD simulations were carried out with the Amber20 suite of programs<sup>53-54</sup> using the GPU-accelerated version of PMEMD<sup>55-56</sup> by following an established procedure.<sup>46</sup> We applied the GAFF2 force field<sup>57</sup> in all simulations. The structures were solvated in a cubic box of TIP3P<sup>45</sup> or OPC<sup>47</sup> water molecules. The systems comprising different tacticity and intra-crosslink chain lengths were solvated such that the distance between the boundary of the box and the closest solute atom was at least 12 Å. For the oligomeric and crosslinked pVCL systems with a variable amount of okanin, we employed PACKMOL<sup>58</sup> to randomly place okanin molecules within a box comprising ~102,900 water molecules, where the box is centered at the geometric center of the pVCL model. Periodic boundary conditions were applied using the particle mesh Ewald (PME) method<sup>59</sup> to treat long-range electrostatic interactions. Bond lengths involving bonds to hydrogen atoms were constrained by the SHAKE<sup>60</sup> algorithm. The time step for all MD simulations was 2 fs, and a direct-space non-bonded cutoff of 8 Å was applied.

Geometric analyses of the trajectories were performed with pytraj<sup>61</sup> and CPPTRAJ.<sup>62</sup> To investigate the properties of pVCL interacting with okanin, we determined key characteristics such as the radius of gyration ( $R_g$ ) of the pVCL and the contacts of the okanin with the pVCL. We define a contact by a distance cutoff, i.e., as any heavy atom of the okanin within 6 Å of any atom of the pVCL. Furthermore, we consider okanin with at least five contacts “adsorbed” and with > 475 contacts “bound” (see next section).

**Free energy calculations.** Following an established procedure<sup>46</sup>, we estimate the binding free energy for the adsorption/binding of okanin to the pVCL microgel using the molecular mechanics Poisson-Boltzmann surface area (MM-PBSA)<sup>63-66</sup> approach. Therefore, we estimate the changes in the effective energy ( $\Delta E_{MM} + \Delta G_{solvation}$ ) and approximate the changes in configurational

315 entropy of the solutes ( $\Delta S_{\text{config}}$ ) upon binding using normal mode analysis<sup>67</sup> (NMA) as  
 316 implemented in MM-PBSA.py.<sup>68</sup> Thus,  $\Delta G_{\text{binding}}$  is defined as depicted in eq. 4:

$$\Delta G_{\text{binding}} = \Delta E_{\text{MM}} + \Delta G_{\text{solvation}} - T\Delta S_{\text{config}} \quad \text{eq. 4}$$

317  $E_{\text{MM}}$  is the sum of bonded and non-bonded molecular mechanics energies (eq. 5):

$$E_{\text{MM}} = \sum_{\substack{\text{bonds} \\ \text{atoms}}} E_{\text{bond}} + \sum_{\text{angles}} E_{\text{angle}} + \sum_{\text{torsions}} E_{\text{torsion}} + \sum_{\substack{\text{atoms} \\ i \neq j}} E_{\text{vdW}} + \sum_{\substack{\text{atoms} \\ i \neq j}} E_{\text{electrostatic}} \quad \text{eq. 5}$$

318  $G_{\text{solv}}$  denotes the solvation free energy (eq. 6):

$$G_{\text{solv}} = G_{\text{pol}} + G_{\text{nonpol}} \quad \text{eq. 6}$$

319

320 and changes in the configurational entropy  $\Delta S_{\text{config}}$  are computed as the sum of the changes in  
 321 translational, rotational, and vibrational entropy:

$$\Delta S_{\text{config}} = \Delta S_{\text{trans}} + \Delta S_{\text{rot}} + \Delta S_{\text{vib}} \quad \text{eq. 7}$$

322

323  $G_{\text{pol}}$  is computed by solving the linear Poisson-Boltzmann equation<sup>69-70</sup> using a dielectric  
 324 constant of 4 for the solute and 80 for water.  $G_{\text{nonpol}}$  is decomposed into a repulsive cavitation  
 325 solvation free energy term  $G_{\text{cavity}}$  and an attractive dispersion solvation free energy term  $G_{\text{dispersion}}$ ,  
 326 which are calculated using a term linearly proportional to the molecular volume enclosed by the  
 327 solvent-accessible surface area (SASA) and a surface-based integration method, respectively.<sup>71</sup>  
 328 Finally, for the NMA, we assume that the polymer chains and the okanin molecules obey a rigid-  
 329 rotor model, such that vibrational frequencies of normal modes can be calculated at local minima  
 330 of the potential energy surface, and translational as well as rotational entropies can be calculated  
 331 using standard statistical mechanical equations.<sup>72</sup> As done in previous works, for the NMA, we  
 332 chose GB<sup>HCT</sup><sup>73-74</sup> as a water model, and each snapshot was minimized until the convergence  
 333 criterion of a difference in minimized energies between two steps of  $< 0.001 \text{ kcal mol}^{-1}$  is satisfied.  
 334 We note that the  $\Delta S_{\text{trans}}$  (eq. 7) depends on the solute concentration.<sup>75</sup> Chemical equilibria that do  
 335 not conserve the number of molecules, such as binding reactions, are concentration-dependent.<sup>76-</sup>  
 336 <sup>77</sup> Here, we obtain binding free energies for a standard state of 1 M termed  $\Delta G_{\text{binding}}^0$ . This results  
 337 in a translational entropy for each component that is smaller by  $6.4 \text{ cal mol}^{-1} \text{ K}^{-1}$  than the entropy

value obtained for the standard state of an ideal gas (1 atm, 298.15 K). Finally, the temperature was set to 298 K for all MM-PBSA calculations, regardless of the simulation conditions.

In total, we calculated free energies for all okanin molecules in all seven trajectories of the linear oligomer ( $n_{\text{okanin}}/n_{\text{CU}}=0.14$ ) where a coil-to-globule transition occurred (Figure S12), treating the okanin molecules as independent, following the “one-trajectory approach”.<sup>68</sup> From the 490,000 frames in total (7 trajectories à 10,000 frames and 7 okanin molecules per system), we considered only frames where the okanin is at least adsorbed (> 5 contacts) (in total 281,065 frames) for the MM-PBSA analysis. We found a dependency of  $\Delta G_{\text{binding}}^0$  on the number of contacts formed with the pVCL. For the linear regression, we find a root of 475 contacts. Thus, we consider okanin molecules with > 475 contacts “bound”, as for these conformations, obtaining a negative  $\Delta G_{\text{binding}}^0$  is more probable. The distribution of obtained  $\Delta G_{\text{binding}}^0$  of bound okanin (> 475 contacts, 38,824 frames) is shown in Figure S13.

**Determination of adsorbed/bound/stacked okanin species.** Using contacts between the different moieties, i.e. contacts between okanin and i) the pVCL, ii) other okanin molecules, and iii) both of the aforementioned, it is possible to distinguish between different okanin species in our simulations. For okanin-polymer interactions, the determined threshold of at least 475 contacts for a potentially favorable interaction (see previous section) allows distinguishing *bound* okanin from loosely *adsorbed* okanin for low molar ratios of okanin and pVCL. For higher concentrations, however, we observe an increasing amount of stacked okanin molecules not only in aqueous solution but also onto already adsorbed or bound okanin. Thus, for higher okanin concentrations, the number of okanin molecules bound to the microgel cannot be determined solely from the contacts with the pVCL microgel but also has to include contacts with other okanin molecules. Choosing solely the same cutoff of 475 for the contacts to the microgel and other okanin molecules, however, overestimates the number of stacked okanin molecules within the microgel for higher molar ratios: To exclude okanin molecules that stack in solution, we thus require that at least 250 of the 475 contacts are formed with the pVCL for an okanin molecule to be considered *stacked within the microgel*. In an optimal stacking configuration, when both okanin molecules are parallel and the aromatic rings are placed atop each other, about ~250 contacts are computed for each of the involved okanin molecules. To account for possible deviations from the optimal configuration, we chose a cutoff of >200 contacts for the identification of okanin molecules involved in *stacking in solution*. Based on this classification scheme, we determined the amounts of bound and adsorbed okanin within the first layer on the microgel, okanin stacked within the microgel or in solution, and free okanin.

371 **Quantification of okanin during release simulations in water and water/ethyl acetate.** To  
372 elucidate the co-solvent-triggered release, we selected the last frames from the simulations of the  
373 crosslinked systems with an okanin/CU molar ratio of 0.04 and 0.28. All molecules within 6 Å of  
374 the pVCL microgel were kept, and all other molecules were discarded. Consecutively, the systems  
375 were re-solvated using either pure water or a saturated water/ethyl acetate solution. The resulting  
376 systems were neutralized again by adding Na<sup>+</sup> or Cl<sup>-</sup> ions as needed. All okanin molecules with  
377 > 475 contacts at the first frame of the release simulations are regarded as “bound” and are traced  
378 through the 1 μs-long simulations. Every okanin molecule not at least adsorbed, i.e., shows >5  
379 contacts, for 98.9% of the time is considered released. Therefore, the relative amount of okanin  
380 released corresponds to the number of released okanin molecules relative to the okanin molecules  
381 initially considered bound.

382 **Co-solvent triggered release of okanin in seedling assays.** Seedlings of the C<sub>4</sub>-weed  
383 *Amaranthus retroflexus* were germinated on paper in the dark and subsequently incubated in the  
384 light for 24 h before treatment. Treatment was performed with buffer (2.4% DMSO in water), 10%  
385 AcOH, 9.4% EtOAc, p(VCL/GMA<sub>shell</sub>) microgels without okanin, p(VCL/GMA<sub>shell</sub>) microgels  
386 saturated with okanin, p(VCL/GMA<sub>shell</sub>) microgels saturated with okanin and EtOAc as a solvent-  
387 release trigger, p(VCL/GMA<sub>shell</sub>) microgels saturated with okanin and AcOH as a solvent-release  
388 trigger, and a buffer solution saturated with okanin. Seedling length was measured after 2 days  
389 with n=20 per treatment. The significance between test results was evaluated using a two-sided  
390 Mann-Whitney U test.

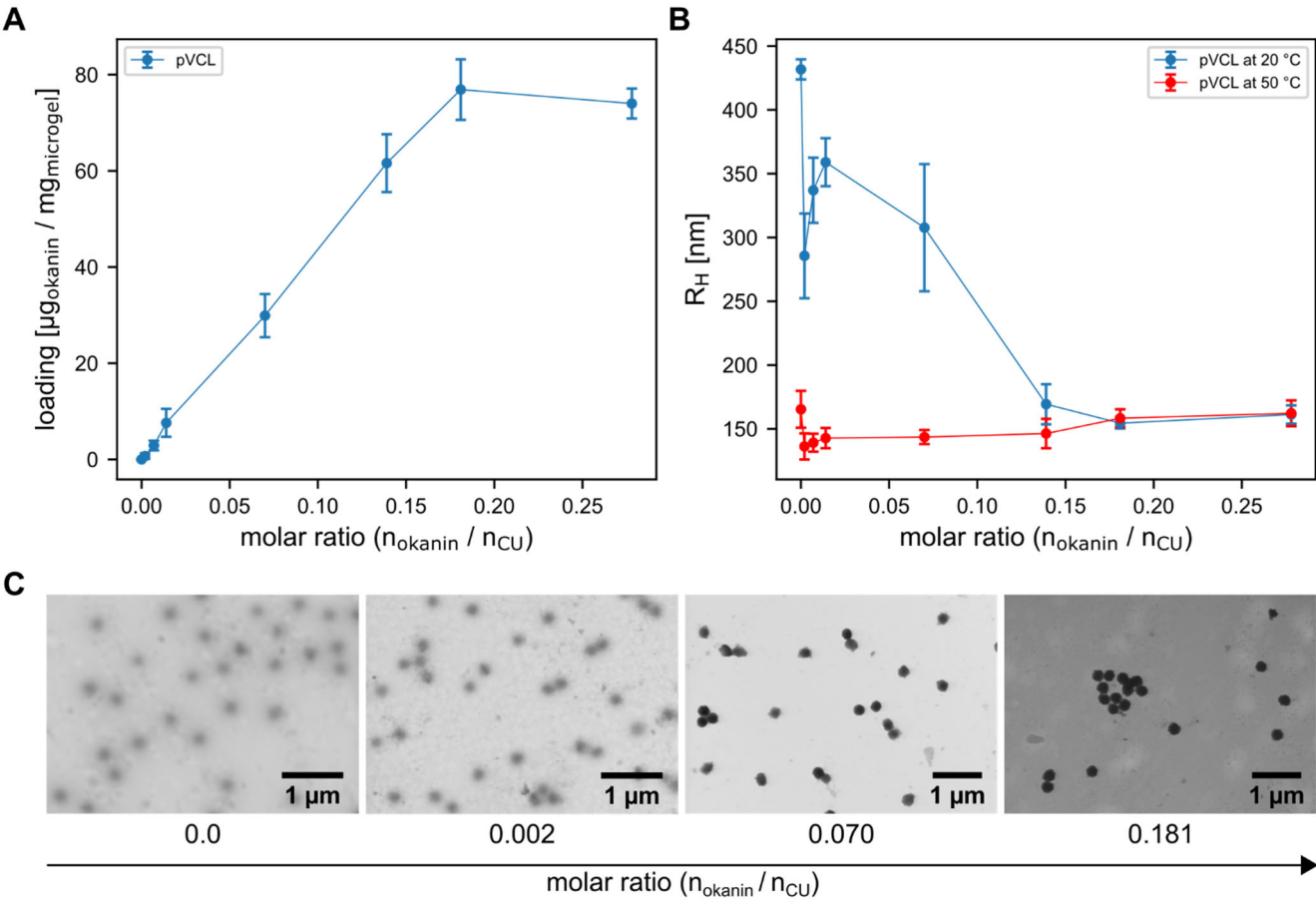
391 **Co-solvent triggered release of okanin in leaves of adult *A. retroflexus* plants, measured**  
392 **by relative photosynthetic activity.** Treatment was performed with buffer (2.4% DMSO in  
393 water), 10% AcOH, 9.4% EtOAc, 10-120 p(VCL/GMA<sub>shell</sub>) microgels without okanin,  
394 p(VCL/GMA<sub>shell</sub>) microgels saturated with okanin, p(VCL/GMA<sub>shell</sub>) microgels saturated with  
395 okanin and EtOAc as a solvent-release trigger, p(VCL/GMA<sub>shell</sub>) microgels saturated with okanin  
396 and AcOH as a solvent-release-trigger, and a buffer solution saturated with okanin. An area of  
397 6 cm<sup>2</sup> was treated per leaf and analyzed after 5 days. Carbon Dioxide Response Curves were  
398 measured with a LiCOR6400 XT portable photosynthesis system. Photosynthetic activity before  
399 treatment was taken for reference.

## 4 Results and Discussion

**DLS, STEM, and AFM reveal that okanin triggers the collapse of the pVCL microgel and leads to a rigidification of the particle.** As shown in previous works,<sup>30-31</sup> polyphenolic compounds form strong interactions with pVCL chains, e.g., tannic acid can be used for supramolecular crosslinking of pVCL. Therefore, pVCL-based microgels depict suitable candidates for use as carriers for the herbicide okanin. To determine the okanin loading capacity of the pVCL microgel, the initial molar ratio between okanin and the constitutional units of the microgel ( $n_{\text{okanin}}/n_{\text{CU}}$ ) was varied, and the loading was determined via UV/Vis. A baseline correction of the UV/Vis spectra was performed to account for the absorbance caused by the turbidity of the microgel solution. The spectra of unloaded microgels cannot be used as a baseline since the turbidity increases with the molar ratio (Figure 1B). As the absorbance of the microgel dispersion decreases exponentially with the wavelength, we investigated using an exponential baseline instead of a linear one (Figure S8). We found that the exponential baseline correction (eq. 1-eq. 3) yields results that are more accurate. The UV/Vis spectra before and after baseline correction are depicted in Figure S6. The loading of the pVCL microgel in relation to the initial okanin concentration is depicted in Figure 3A. The loading increases linearly until a molar ratio of 0.18. Between molar ratios of 0.18 and 0.28, the amount of loaded okanin remains constant at  $\approx 75 \mu\text{g}/\text{mg}$ . This observation correlates with the precipitation of okanin for molar ratios above a molar ratio of 0.18 indicating the saturation of the solution. The most efficient loading is achieved at a molar ratio of 0.18 as the loading is converged.

To elucidate the impact of the amount of loaded okanin on the swelling of the microgels,  $R_{\text{H}}$  was determined by DLS at 20 °C ( $R_{\text{H}, 20\text{ °C}}$ ) and 50 °C ( $R_{\text{H}, 50\text{ °C}}$ ) depending on the initial okanin concentration (Figure 3B).  $R_{\text{H}, 20\text{ °C}}$  and  $R_{\text{H}, 50\text{ °C}}$  both converge to a size of  $\approx 160 \text{ nm}$  at a molar ratio of 0.18. Independent of the temperature, fully loaded microgels are collapsed, while unloaded microgels show a temperature depending swelling (Figure S2). Therefore, the binding of okanin may lead to the loss of the microgel's thermo-responsiveness. Surprisingly,  $R_{\text{H}, 20\text{ °C}}$  and  $R_{\text{H}, 50\text{ °C}}$  do not continuously converge with increasing molar ratios. At a very low molar ratio ( $n_{\text{okanin}}/n_{\text{CU}} = 0.002$ ),  $R_{\text{H}, 20\text{ °C}}$  and  $R_{\text{H}, 50\text{ °C}}$  both decrease. At higher molar ratios,  $R_{\text{H}, 20\text{ °C}}$  increases again until reaching a molar ratio of 0.01 before the collapse of the microgels is triggered, whereas  $R_{\text{H}, 50\text{ °C}}$  remains approximately constant ( $\approx 140\text{-}160 \text{ nm}$ ) with increasing molar ratio.





431

432 **Figure 3:** Influence of the loading of okanin on the hydrodynamic radius, the thermo-responsiveness, and the  
433 morphology of pVCL microgels. **A** Loading of okanin into pure pVCL microgels determined by UV/Vis  
434 for varying molar ratios  $n_{\text{okanin}}/n_{\text{CU}}$ . **B**  $R_H$  of pVCL microgels before and after loading with okanin as  
435 determined by DLS at 20 °C and 50 °C for varying  $n_{\text{okanin}}/n_{\text{CU}}$  ratios. **C** Exemplary STEM images of a  
436 pVCL microgel for varying  $n_{\text{okanin}}/n_{\text{CU}}$  ratios.

437 The morphology of the microgels for varying okanin concentrations during loading was  
438 investigated with STEM images (Figure 3C). A rigidification of the microgels upon loading is  
439 observed, in line with the collapse of the microgels. Two distinct morphologies are observed for a  
440 molar ratio of 0.070. This might be indicative of an inhomogeneous loading within the microgels  
441 (core/shell) with different impacts on the particles' size. While the loading of the core leads to  
442 neglectable changes in particle size, the collapse of the dangling ends can cause a substantial size  
443 decrease. Therefore, at a molar ratio of 0.070, some microgels might already be nearly saturated  
444 whereas others are not, potentially leading to the wide structural variety for this okanin/CU ratio.  
445 This observation also explains the high standard deviation observed in DLS for a molar ratio of  
446 0.070 (Figure 3B). Surprisingly, the microgels shown in the STEM images already seem to be  
447 collapsed at a molar ratio of 0.070, which opposes the swelling determined by DLS (Figure 3B).  
448 The drying of the microgels during the preparation of STEM samples can explain this difference.

The removal of the solvent locally increases the okanin concentration and, thus, interactions between okanin and pVCL, that way enhancing the collapse.

To confirm the different effects on the size and morphology at low and high molar ratios observed by DLS, STEM and AFM images of the pVCL microgel with varying concentrations of okanin during the loading were recorded (Figure S14). Height profiles ( $H_{AFM}$ ) and the radius ( $R_{AFM}$ ) of the microgels were obtained (Table 1). Due to the stiffness of the loaded microgels, the cantilever moved the particles during the AFM, making it impossible to determine the particles' width with this method. Instead, the width of saturated microgels was determined from STEM images (Figure 3C). Histograms are shown in Figure S15. Due to the rigid structure of the saturated microgels, the radius of the particle ( $R_{STEM}$ ) can be determined, which is usually not accessible for diffuse microgels using STEM, as they spread on the surface.

**Table 1:** Okanin loadings and dimensions of the pVCL microgel for varying molar ratios of okanin/CU determined by DLS, AFM, and STEM.

Molar ratio ( $n_{okanin}/n_{CU}$ )	Okanin loading [ $\mu g_{okanin}/mg_{microgel}$ ]	$R_{H, 20\text{ }^{\circ}C}$ [nm]	$PDI_{20\text{ }^{\circ}C}$ [-]	$R_{H, 50\text{ }^{\circ}C}$ [nm]	$PDI_{50\text{ }^{\circ}C}$ [-]	$R_{STEM}$ [nm]	$R_{AFM}$ [nm]	$H_{AFM}$ [nm]
0.000	0	$432 \pm 8$	$0.159 \pm 0.023$	$165 \pm 14$	$0.162 \pm 0.014$	n.a. <sup>1</sup>	$290 \pm 36$	$96 \pm 10$
0.002	$0.7 \pm 0.6$	$286 \pm 33$	$0.111 \pm 0.044$	$136 \pm 10$	$0.081 \pm 0.019$	n.a. <sup>1</sup>	$277 \pm 34$	$68 \pm 6$
0.070	$29.9 \pm 4.5$	$308 \pm 50$	$0.215 \pm 0.172$	$144 \pm 5$	$0.050 \pm 0.031$	$115 \pm 13$	n.a. <sup>2</sup>	$138 \pm 17$
0.181	$76.9 \pm 6.3$	$154 \pm 4$	$0.041 \pm 0.031$	$158 \pm 7$	$0.036 \pm 0.019$	$117 \pm 7$	n.a. <sup>2</sup>	$257 \pm 15$

<sup>1</sup>not available due to the diffuse morphology of the microgel.

<sup>2</sup>not available due to the rigid, spherical morphology of the microgel.

Compared to the untreated microgel with  $H_{AFM}$  and  $R_{AFM}$  of 96 nm and 290 nm, respectively, okanin loading at a molar ratio of 0.002 leads to a decrease in  $H_{AFM}$  and  $R_{AFM}$  to 68 nm and 277 nm, respectively. This observation agrees with the decrease of  $R_{H, 20\text{ }^{\circ}C}$  at 0.002 and indicates the collapse of the microgel's shell. At the molar ratio of 0.070,  $H_{AFM}$  increases again to 138 nm, which is in line with the observed increase in  $R_{H, 20\text{ }^{\circ}C}$ . The deviation from  $2 \times R_{STEM} = 230$  nm indicates that the microgels are still at least partly spread on the surface, in line with the previously described drying phenomenon. Finally, saturated microgels loaded at the high molar ratio of 0.181 show a height  $H_{AFM}$  of  $257 \pm 15$  nm, which is in good agreement with  $2 \times R_{STEM} = 234 \pm 14$  nm, supporting the formation of a rigid sphere. The height increase is caused by the collapse and rigidification as the morphology continuously transitions from a spreading structure to a sharply defined spherical one.

Observed changes in the microgel's size and morphology might be caused by the formation of non-covalent okanin-mediated intra-chain crosslinks. The deviation between loading at low and high molar ratios might be caused by the structural inhomogeneity of the microgel, i.e., the loosely

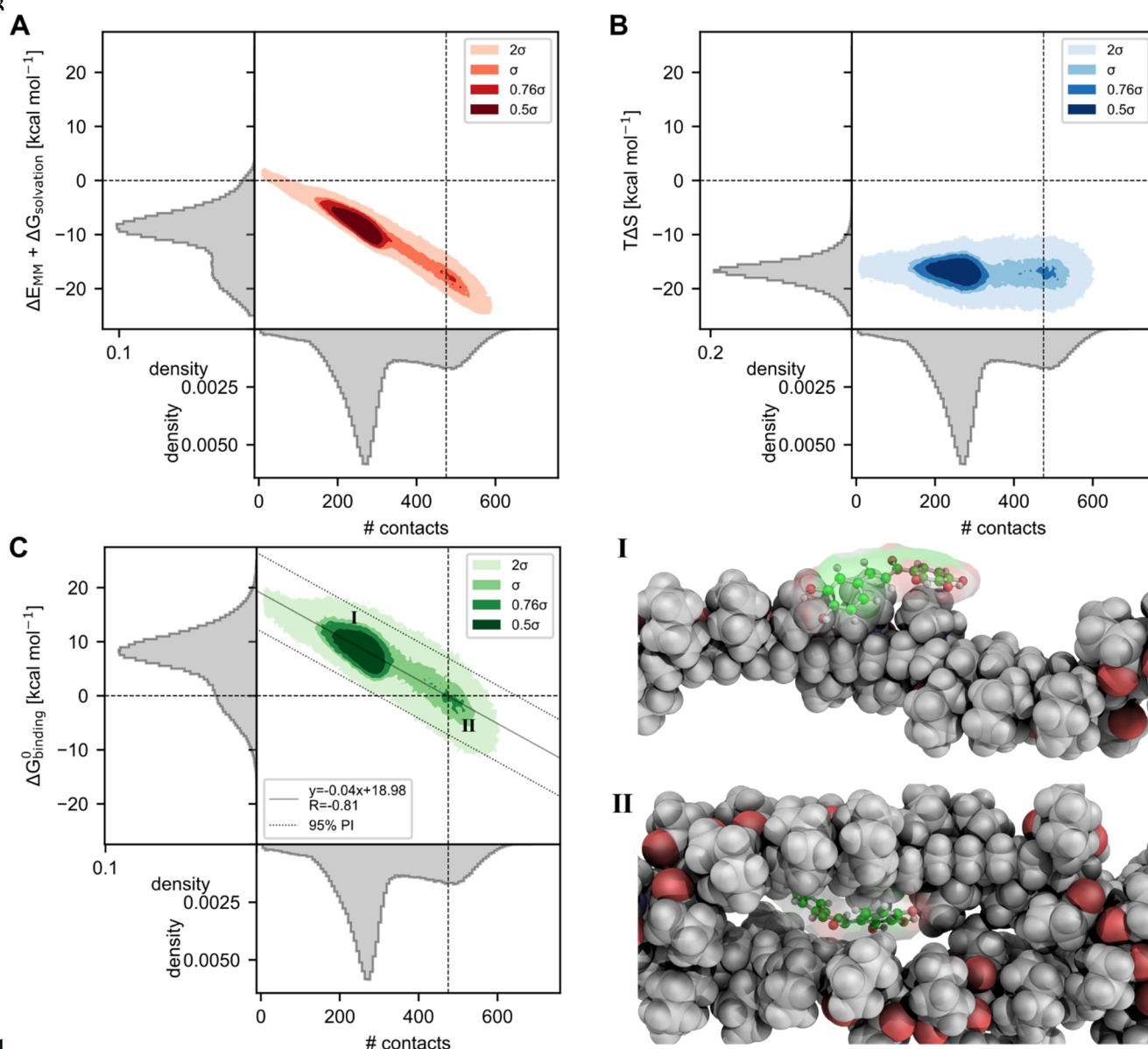
crosslinked shell and the densely crosslinked core. While loading the core might lead to a slight decrease in the microgel's size, loading the shell and the accompanying collapse of the dangling chains might lead to the opposite effect. The strong decrease in size at very low molar ratios, however, might be explained by an increase in ionic strength, as it has been shown that ions and other osmolytes influence the phase transition of pVCL.<sup>78-79</sup> To validate our hypotheses and elucidate the interactions of okanin with the pVCL microgel at the atomistic scale, we performed molecular dynamics simulations.

**Molecular dynamics simulations reveal a collapse of linear pVCL and compaction of crosslinked pVCL upon okanin loading.** To elucidate the structural changes of the pVCL microgel upon okanin loading, we performed okanin loading simulations of linear and crosslinked pVCL representing the shell and the core of the microgel, respectively (Figure 2). For linear pVCL and a molar ratio ( $n_{\text{okanin}}/n_{\text{CU}}$ ) of 0.14, we observed a coil-to-globule transition triggered by okanin (Figure S12, two and five out of ten trajectories for simulations at 293 K and 313 K, respectively). Interestingly, with higher amounts of okanin (molar ratio of 0.56 and 1.12), fewer coil-to-globule transitions are observed (Figure S12). In general, the collapse of linear pVCL leads to a decrease in particle size (Figure S12). For crosslinked pVCL, however,  $R_g$  and, thus, the size of the polymer increases slightly (Figure S16 to Figure S18) as the crosslinked pVCL forms porous structures (Figure S19) with an increasing amount of okanin.

Visual inspection of the okanin binding to the pVCL models revealed that the binding can be categorized into two types (Figure S20). The first type describes the frequent short-living adsorption of the okanin to only one polymer chain. The second type comprises molecules that are long-term bound to at least two chains, which may also be formed by a folded linear chain. To quantify the energetics of the two distinct binding types, we performed MM-PBSA calculations using trajectories of the linear pVCL, where a coil-to-globule transition occurred, as these trajectories comprise both types of interactions.

**The collapse of linear pVCL and compaction of crosslinked pVCL is driven by minimizing the free energy of okanin binding.** We performed MM-PBSA calculations on 490,000 frames from the simulation of a linear pVCL chain with a  $n_{\text{okanin}}/n_{\text{CU}}$  ratio of 0.14. We decided to use the results from the MM-PBSA analysis of okanin binding at a low  $n_{\text{okanin}}/n_{\text{CU}}$  ratio where stacking is not observed to focus on pure okanin microgel interactions. Considering MM-PBSA is an end-point method for estimating binding free energies, we only used frames where the okanin is at least adsorbed to the pVCL. The results of the MM-PBSA analysis for the adsorption and binding of okanin are depicted in Figure 4.

513



514

**Figure 4:** Two-dimensional histograms of the binding free energy of okanin to the linear pVCL 50mer and its components (changes in the gas phase energy and solvation free energy ( $\Delta E_{MM} + \Delta G_{solvation}$ , **A**) and changes in the configurational entropy of the solutes (TΔS, **B**)) in relation to the number of formed contacts. The binding free energy ( $\Delta G_{binding}^0$ , **C**) of okanin to the pVCL polymer shows an inverse linear correlation (regression line shown solid, 95% prediction interval shown dotted, Pearson correlation coefficient and linear equation are depicted in the corresponding legend) with the number of formed contacts. Exemplary binding poses are shown for adsorbed okanin (**I**, < 475 contacts,  $\Delta G_{binding}^0 > 0$ ) and bound okanin (**II**, > 475 contacts,  $\Delta G_{binding}^0 < 0$ ). The MM-PBSA analysis was performed for trajectories of the linear pVCL 50mer, in which a collapse of the chain was observed; only frames where okanin formed contacts to pVCL were considered.

The MM-PBSA analysis reveals an inverse correlation of  $\Delta E_{MM} + \Delta G_{solvation}$  for an increasing number of contacts (Figure 4A), i.e., the more contacts between the okanin and the pVCL, the more negative and, hence, favorable  $\Delta E_{MM} + \Delta G_{solvation}$ . Changes in the configurational entropy of the solutes (TΔS) upon the binding of okanin, however, are nearly independent of the number of formed contacts (Figure 4B). Therefore, the resulting change in binding free energy,  $\Delta G_{binding}^0$ , shows an inverse correlation with the number of formed contacts, too. A linear correlation reveals

that at  $\approx 475$  contacts, the unfavorable change in configurational entropy is outbalanced by the favorable change in  $\Delta E_{\text{MM}} + \Delta G_{\text{solvation}}$ . Note that for 38,824 frames where okanin has  $> 475$  contacts with the pVCL, the  $\Delta G_{\text{binding}}^0$  values are normally distributed with a mean value of  $-2.68 \text{ kcal mol}^{-1}$  (Figure S13), indicating converged sampling of that property. The maximum number of contacts observed for the adsorption to a single pVCL chain is  $< 350$  (Figure S21 and Figure S22). Thus, to achieve an energetically favorable binding pose, the okanin needs to be in contact with either at least two separate pVCL chains within a crosslinked pVCL microgel or within a collapsed linear chain. Within the crosslinked pVCL model, this promotes compaction as okanin forms interactions with two chains within the polymer network. For sections of the microgel containing dangling ends and a low crosslink density, comparable to the simulation using the linear pVCL oligomer, the binding of okanin leads to a substantial decrease in the particle size, as okanin promotes the coil-to-globule transition of single chains to achieve an energetically favorable binding mode.

The decomposition of  $\Delta E_{\text{MM}}$  and  $\Delta G_{\text{solvation}}$  yields further insights into the nature of interactions between the okanin and pVCL.  $\Delta E_{\text{MM}}$  is decomposed into van der Waals ( $\Delta E_{\text{vdW}}$ ) and electrostatic energies ( $\Delta E_{\text{eel}}$ ) (eq. 5) as internal energies cancel due to the used one-trajectory approach. Upon okanin binding, both  $\Delta E_{\text{vdW}}$  and  $\Delta E_{\text{eel}}$  become increasingly favorable with an increasing number of formed contacts (Figure S23). Although both terms show favorable energies for the binding of okanin,  $\Delta E_{\text{vdW}}$  contributes  $\sim 2.5$  times more ( $\sim -34.3 \text{ kcal mol}^{-1}$  at 475 contacts, Figure S23A) than  $\Delta E_{\text{eel}}$  ( $\sim -13.3 \text{ kcal mol}^{-1}$  at 475 contacts, Figure S23B). As expected, both  $\Delta E_{\text{vdW}}$  and  $\Delta E_{\text{eel}}$  contribute more favorably to the binding of okanin with an increasing number of contacts between okanin and the oligomer.

Changes in  $G_{\text{solvation}}$  upon binding can be decomposed into changes in polar  $G_{\text{pol}}$  and nonpolar  $G_{\text{nonpol}}$  contributions (eq. 6), where  $G_{\text{nonpol}}$  can be further decomposed into a repulsive cavitation solvation free energy term  $G_{\text{cavity}}$ , and an attractive dispersion solvation free energy term  $G_{\text{dispersion}}$ . With an increasing number of contacts,  $\Delta G_{\text{pol}}$  decreases linearly, i.e., okanin binding becomes more favorable with an increasing number of contacts (Figure S24A). The free energy needed for the endergonic processes of cavity formation (Figure S24B) and dispersion (Figure S24C), however, outweighs the aforementioned exergonic polar contribution, resulting in an overall unfavorable  $\Delta G_{\text{solvation}}$ .

To evaluate whether the binding is mainly dominated by polar or nonpolar interactions, we calculated the sum of the electrostatic terms, i.e.,  $\Delta E_{\text{eel}}$  and  $\Delta G_{\text{pol}}$ , and the nonpolar ones, i.e.,  $\Delta E_{\text{vdW}}$  and  $\Delta G_{\text{nonpol}}$ . The former sum is favorable with  $-38.9 \text{ kcal mol}^{-1}$  at 475 contacts, whereas the latter is unfavorable with  $22.6 \text{ kcal mol}^{-1}$  at 475 contacts due to  $\Delta G_{\text{nonpol}}$ . Hence, according to

the MM-PBSA analysis, polar interactions are the driving factor for okanin binding. Thus, we predict that the substitution or incorporation of moieties carrying additional (partially) charged moieties or hydrogen bond acceptors shall increase the okanin loading capacity of the microgel. This finding is well in line with using tannic acid as a supramolecular crosslinker for pVCL and other hydrogels, where hydrogen bonds were identified as the driving force for the physical crosslink.<sup>30, 80</sup>

**MD simulations allow the quantification of different okanin species and interactions with respect to the okanin concentration in solution during loading.** In our MD simulations, we identified increasing stacking interactions (Figure 5A-D, Figure S25) between the okanin molecules with increasing okanin concentrations. The stacking is observed for okanin in solution (Figure 5A, B, Figure S26) as well as for already adsorbed or bound okanin (Figure 5C, D, Figure S27 to Figure S29). Thus, a second okanin molecule might be either stacked onto an adsorbed okanin molecule (Figure 5C) or incorporated in the polymer-okanin-polymer configuration (Figure 5D) previously identified as bound okanin based on free energy calculations (Figure 4). The stacking of okanin inside the microgel might underlie the increased release of okanin from saturated microgels. The fraction of okanin found in a stacked configuration approximately linearly correlates with an increasing  $n_{\text{okanin}}/n_{\text{CU}}$  ratio (Figure 5E (blue line)). In preliminary tests, we aimed at determining the amount of bound okanin as those with  $> 475$  contacts. However, with increasing  $n_{\text{okanin}}/n_{\text{CU}}$  ratio, this led to decreasing amounts of bound okanin (Figure 5E (green line) and Figure S27), although the number of adsorbed okanin molecules is less affected (Figure 5E (yellow line) and Figure S28). Including contacts to other okanin molecules (i.e.,  $> 475$  contacts formed with the polymer and other okanin molecules with at least 250 contacts to the polymer) allows distinguishing bound and/or stacked okanin in the microgel (Figure 5E (red line) and Figure S29) from adsorbed okanin or okanin stacked in solution in simulations with higher okanin concentrations. Additionally to the contact-based identification and quantification of stacked okanin, we monitored the increase in stacking interactions between the okanin molecules using radial distribution functions ( $g(r)$ ) of the distances between the aromatic rings.  $g(r)$  substantially increases around 4 Å for molar ratios above 0.28 (Figure S30), which supports the increased number of stacking interactions at high okanin concentrations.

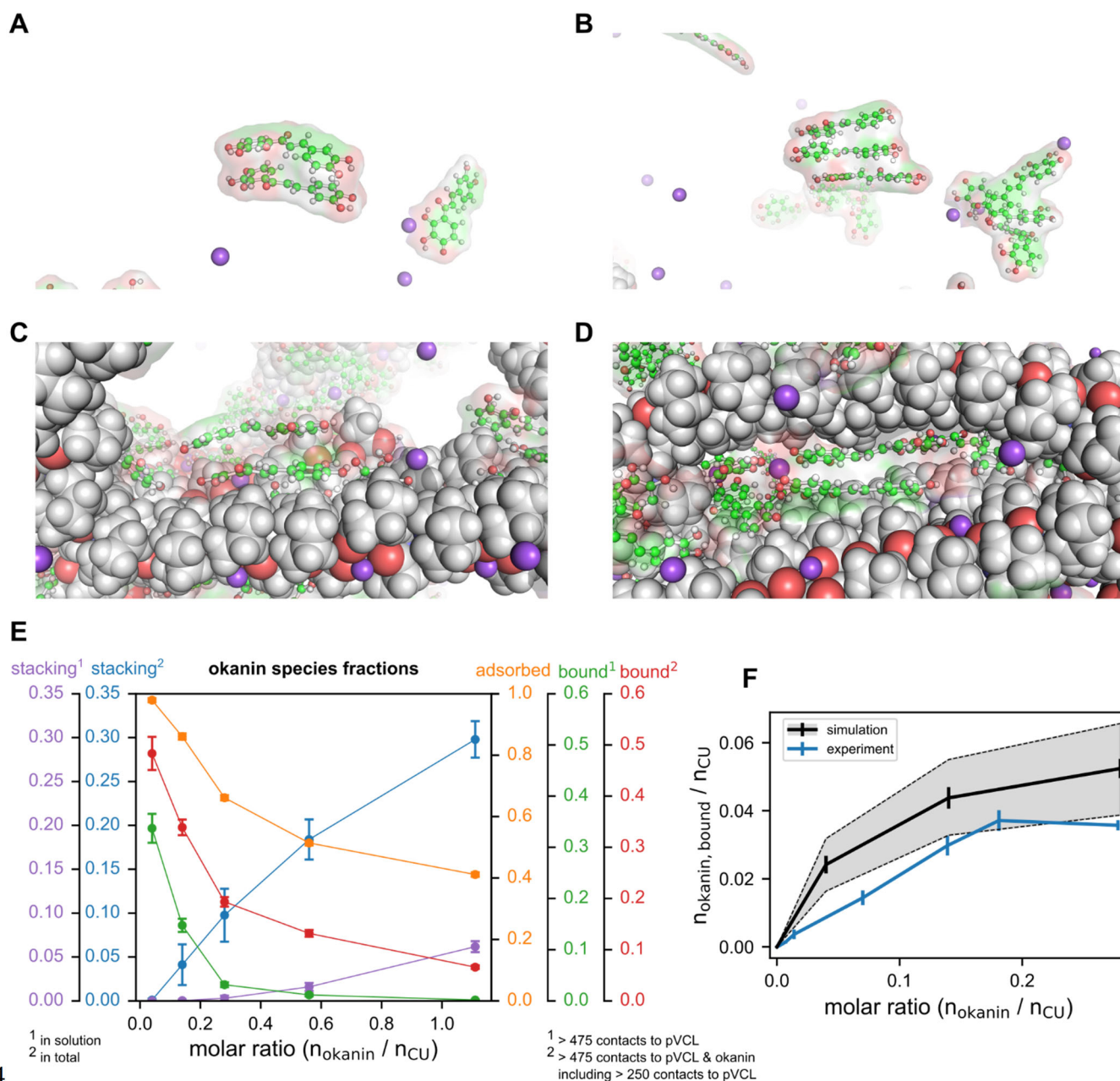


**Figure 5:** Quantification of different okanin species and interactions. Okanin stacks in solution (**A** two molecules, **B** three molecules), on adsorbed okanin (**C**), and within a bound state (**D**) at a high molar ratio ( $n_{\text{okanin}}/n_{\text{CU}} = 1.11$ ). **E** Quantification of okanin species. Okanin species fractions are given in relation to the overall number of okanin molecules within the respective system. With increasing okanin concentration, the fraction of okanin molecules in a stacking configuration in solution increases linearly for molar ratios above 0.28 (purple), while the overall fraction including stacking to bound/adsorbed okanin (blue) increases linearly for all molar ratios. The fraction of adsorbed (yellow), bound (green), and stacked within the microgel (red) okanin decreases with increasing okanin concentration. **F** Comparison of experimentally determined bound okanin per constitutional unit ( $n_{\text{okanin,bound}}/n_{\text{CU}}$ ) with okanin considered bound and/or stacked within the microgel (> 475 contacts to pVCL or > 475 contacts and at least 250 contacts formed with pVCL) in MD simulations. The grey shaded area depicts the uncertainty related to a change of the cutoff of  $\pm 25$  contacts (i.e., 450 and 500 contacts for the upper and lower bound, respectively), which corresponds to a change of the computed binding free energy of approximately  $\pm 1$  kcal mol<sup>-1</sup>.



609 In conclusion, for an increasing  $n_{\text{okanin}}/n_{\text{CU}}$  ratio, okanin-okanin interactions become  
610 increasingly important for the behavior in solution for molar ratios above 0.28, however, stacking  
611 on already adsorbed or bound okanin is preferred at all simulated molar ratios (Figures S24-28).  
612 In solution, the increase in okanin-okanin stacking potentially leads to experimentally observed  
613 precipitation of the dispersed okanin. For low okanin concentrations, we found that okanin is  
614 primarily bound between two polymer chains as this binding mode is energetically favorable. For  
615 high concentrations, however, we observe stacking of okanin onto already adsorbed okanin,  
616 replacing one polymer chain in the polymer-okanin-polymer structure. Furthermore, we observe  
617 the incorporation of an additional okanin molecule in the polymer-okanin-polymer structure.

618 Considering these cases, the amount of bound and/or stacked okanin within the microgel  
619 ( $> 475$  contacts to pVCL or  $> 475$  contacts to pVCL and at least 250 contacts formed with the  
620 polymer) observed in simulations with increasing okanin concentration semi-quantitatively  
621 matches the experimentally determined loadings, particularly for  $n_{\text{okanin}}/n_{\text{CU}}$  ratios  $> 0.14$   
622 (Figure 5F). The slight overestimation of bound okanin in the simulations might be due to different  
623 length scales of the microgel particles with respect to the experiment, which may impact the access  
624 of okanin to the microgel or the egress in comparison to experimental loading/washing. Another  
625 reason might be the loss of okanin during the washing steps performed in the experimental loading  
626 process (Figure 1).

627 **Incorporating GMA into pVCL microgels increases the overall loading capacity without**  
628 **changing the saturation concentration.** To improve the loading capacity of pVCL-based  
629 microgels, we investigated the nature of the interactions between okanin and the pVCL microgel  
630 by MM-PBSA calculations. The calculations revealed that polar interactions are the driving factors  
631 for okanin binding to the microgel. Thus, we predicted that incorporating moieties carrying  
632 additional (partially) charged moieties or an increased number of hydrogen bond acceptors might  
633 benefit okanin loading.

634 To validate our hypothesis, we investigated the influence of GMA incorporation (10 mol%)  
635 on the loading capacity, as it contains more potential hydrogen bond acceptors.<sup>32</sup> To determine the  
636 influence of the localization of GMA, GMA was incorporated into the shell (p(VCL/GMA<sub>shell</sub>))  
637 and the core (p(VCL/GMA<sub>core</sub>)). The amount of okanin-loaded into the p(VCL-co-GMA)  
638 microgels was determined analogously to pVCL using UV/Vis spectroscopy. The spectra are  
639 shown in Figure S31 and Figure S32 and the results are depicted in Figure 6A.



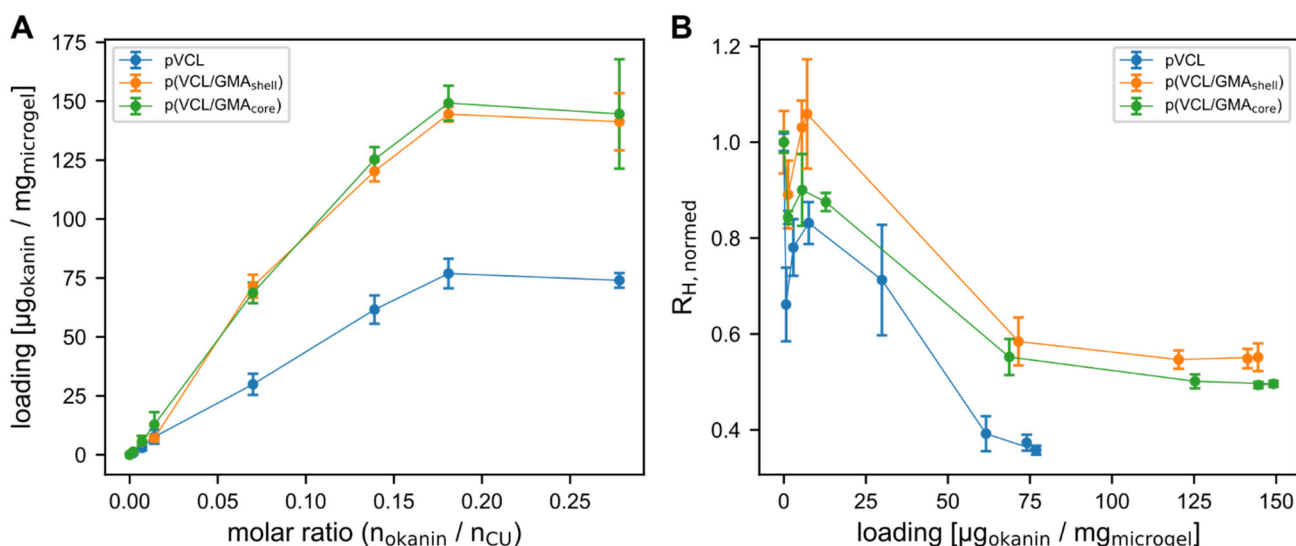


**Figure 6:** Determined okanin loading capacity of pVCL and p(VCL-co-GMA) microgels and effect on the microgel size. **A** Loading of okanin into pVCL and p(VCL-co-GMA) microgels determined by UV/Vis in dependency of the molar ratio  $n_{\text{okanin}}/n_{\text{CU}}$ . **B**  $R_{\text{H, norm}}$  of pVCL and p(VCL-co-GMA) microgels determined by DLS at 20 °C.

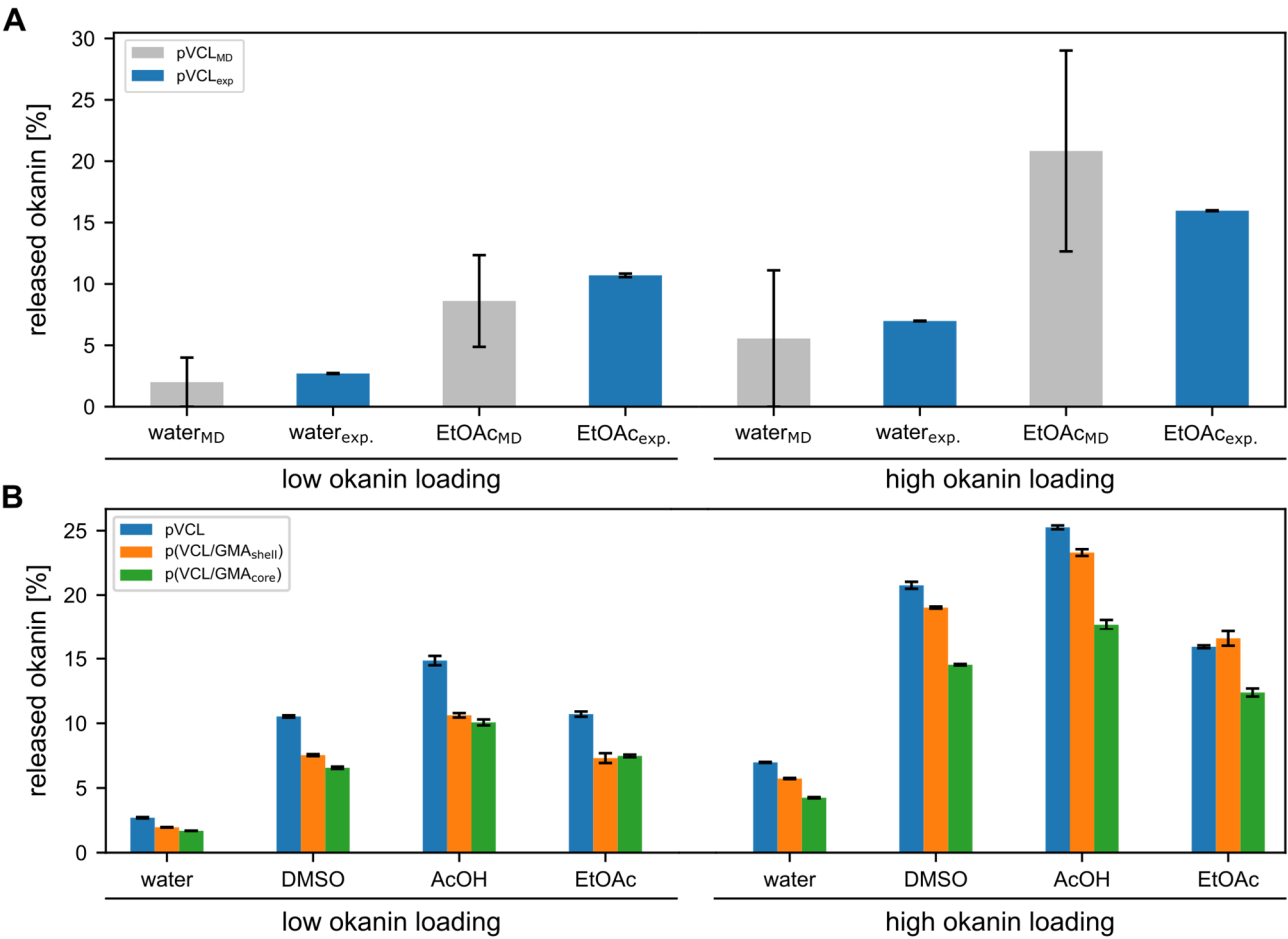
The loading increases linearly for both p(VCL-co-GMA) microgels analogous to the pure pVCL microgel. Saturation of the microgels is achieved at a molar ratio of 0.18, independent of the microgel variant. The loading capacity of both p(VCL-co-GMA) microgels is  $\approx 150 \mu\text{g}/\text{mg}$  and, thus, two-fold as large as the loading capacity of the pure pVCL microgel ( $\approx 75 \mu\text{g}/\text{mg}$ ). A high amount of precipitate during the loading of okanin into p(VCL-co-GMA) at the highest okanin concentration led to larger errors in the amount of loaded okanin. For this reason, loading at even higher okanin concentrations is not accessible through experiment.

Surprisingly, the localization of the GMA within the microgel does not influence the loading of okanin as the loading profiles of p(VCL/GMA<sub>shell</sub>) and p(VCL/GMA<sub>core</sub>) are virtually identical (Figure 6A). We hypothesize that localization of the GMA-rich polymer segments in the microgel shell will enhance their accessibility and make okanin loading more efficient.  $R_{\text{H, 20 °C}}$  and  $R_{\text{H, 50 °C}}$  were determined for both p(VCL-co-GMA) microgels by DLS (Table S13). To determine if the collapse/compaction depends on the amount of bound okanin independent of the composition,  $R_{\text{H, 20 °C}}$  for all three microgel variants is plotted as a function of the loading and normalized to the size of the unloaded microgel, yielding the normalized hydrodynamic radius  $R_{\text{H, norm}}$  (Table S13). The overall trend of  $R_{\text{H, norm}}$  is similar for all three microgel variants (Figure 6B). The collapse of the GMA-containing microgels was also confirmed by AFM images (Figure S33 and Figure S34) and STEM images (Figure S35 to Figure S37). Analogous to the loading profile, the localization of the GMA within the microgels does not influence the changes in the microgel's size. Interestingly, the collapse of the microgel is triggered at loadings of 60 - 75  $\mu\text{g}/\text{mg}$ , independent of the microgel composition. This is indicative of a critical amount of okanin

necessary to mediate non-covalent inter-chain crosslinks to trigger the collapse of the microgels. Moreover, further loading of okanin is observed even after the full collapse of the microgels. Thus, okanin molecules might bind onto the surface of the microgel at this point, or the collapse of the microgel might generate other sites within the microgel that are favorable for the binding of okanin.

**Experiments and simulations show that the co-solvent-triggered release of okanin is more efficient than the release in pure water.** For a controlled release of okanin, a suitable trigger is required to manipulate the interactions between okanin and its carrier. Green solvents depict promising candidates to shift the equilibrium between bound and unbound okanin by influencing the intermolecular interactions within the system. As release agents, we chose the green solvents EtOAc, DMSO, and AcOH. DMSO and AcOH are commonly used in agricultural formulations. The EtOAc was chosen as an organic solvent reference and as a benchmark. The co-solvent triggered release from pure pVCL microgels loaded at  $n_{\text{okanin}}/n_{\text{CU}}$  ratios of 0.07 and 0.18 were investigated by adding 9.4 vol.-% of EtOAc to the microgel dispersion. A reference was obtained by adding the same volume of water. The release of okanin in relation to the initial loading was determined via UV/Vis spectroscopy. Simultaneously, we investigated the co-solvent-induced release of okanin in MD simulations (see Quantification of okanin released during release simulations in water and water/ethyl acetate in the Materials and Methods). The comparison of both results is depicted in Figure 7A.

The relative release of pVCL loaded at a lower okanin is also lower than the release from microgels loaded at higher okanin concentration (Figure S38 to Figure S41 for simulation / Figure S42 and Figure S43 for experiments). For a low okanin loading, the release of okanin in water (2.7%) and EtOAc (10.7%) observed in experiments matches the observed release in MD simulations. For the pVCL microgel loaded at a high okanin concentration, 7.0% of the bound okanin molecules are released in water, whereas the release increases to 15.9% for EtOAc. The release observed in MD simulations also matches the experimental results for water and slightly overestimates the release in EtOAc. For the release in water, however, the overall number of released okanin molecules is lower and the desorption event is less likely. Thus, further sampling or increasing the system size might be necessary to further decrease the uncertainty in the estimated amount of released okanin.



697

698 **Figure 7:** Co-solvent-triggered release of okanin in experiments and simulations. **A** Comparison of  
699 experimentally observed okanin release for EtOAc with release observed in MD simulations. The  
700 experimental values are compared to the release in MD simulations observed for microgels loaded at  
701 low okanin loadings ( $n_{\text{okanin}}/n_{\text{CU}} = 0.04$  and  $n_{\text{okanin}}/n_{\text{CU}} = 0.07$  for MD and experiment, respectively) and  
702 high okanin loading ( $n_{\text{okanin}}/n_{\text{CU}} = 0.28$  and  $n_{\text{okanin}}/n_{\text{CU}} = 0.18$  for MD and experiment, respectively).  
703 **B** Experimentally observed okanin release for different co-solvents (DMSO, AcOH, and EtOAc) for  
704 low ( $n_{\text{okanin}}/n_{\text{CU}} = 0.07$ ) and high ( $n_{\text{okanin}}/n_{\text{CU}} = 0.18$ ) okanin concentrations at loading. The initial  
705 loadings were 31.1  $\mu\text{g}/\text{mg}$  and 73.0  $\mu\text{g}/\text{mg}$  for pVCL, 65.7  $\mu\text{g}/\text{mg}$  and 146.0  $\mu\text{g}/\text{mg}$  for  
706 p(VCL/GMA<sub>core</sub>) and 72.3  $\mu\text{g}/\text{mg}$  and 144.2  $\mu\text{g}/\text{mg}$  for p(VCL/GMA<sub>shell</sub>).

707 Besides EtOAc, we investigated the effect of other common green solvents. We chose DMSO  
708 due to the high solubility of okanin and AcOH to probe the influence of a protic solvent. The  
709 results for the release from pVCL as well as p(VCL/GMA<sub>shell</sub>) and p(VCL/GMA<sub>core</sub>) are depicted  
710 in Figure 7B. Both solvents further increase the release compared to EtOAc, with the highest  
711 release observed for AcOH (25.3%). The observed trends for the different solvents are similar for  
712 all microgel variants, irrespective of the okanin concentration during loading. Although the relative  
713 release of okanin is decreased for the p(VCL-co-GMA) microgels, the absolute amount of okanin  
714 released is higher due to higher loading (Figure S43). The decreased relative release for the  
715 p(VCL-co-GMA) microgels compared to the pure pVCL microgel may be due to the okanin  
716 forming stronger interactions with the GMA moieties. Interestingly, the incorporation of GMA in

717 the core decreases the release stronger than in the shell, regardless of the amount of loaded okanin.  
718 This effect, however, is more pronounced for saturated microgels. Thus, we assume that the okanin  
719 is preferentially localized within the GMA-rich sections of the microgel. In the case of  
720 p(VCL/GMA<sub>shell</sub>), the okanin is mainly bound to the shell from which a release is easier, whereas  
721 the release is hindered by diffusive traps in p(VCL/GMA<sub>core</sub>), especially for (partially) collapsed  
722 microgels.

723 **Seedling assays and measurements of relative photosynthetic activity yield**  
724 **proof-of-principle for the application on *A. retroflexus* plants.** Seedlings of the C<sub>4</sub>-weed *A.*  
725 *retroflexus* were germinated on paper and treated with p(VCL-co-GMA) microgels saturated with  
726 okanin, p(VCL/GMA<sub>shell</sub>) microgels saturated with okanin and EtOAc as a solvent-release trigger,  
727 p(VCL/GMA<sub>shell</sub>) microgels saturated with okanin and AcOH as a solvent-release trigger, and a  
728 buffer solution saturated with okanin plus the respective controls (Figure 8A). Treatments with the  
729 unloaded p(VCL/GMA<sub>shell</sub>) microgels, AcOH, and EtOAc either result in insignificant differences  
730 or, for EtOAc, negligible differences compared to the control treated with buffer. All okanin-  
731 containing treatments result in significantly shorter seedlings than the controls. Solvent-triggered  
732 release of okanin yields significantly shorter seedlings than the ones treated solely with  
733 p(VCL/GMA<sub>shell</sub>) microgels saturated with okanin; EtOAc or AcOH as release triggers do not lead  
734 to significantly different results. Buffer saturated with okanin results in the shortest seedling  
735 lengths. Note, however, that we did not test the influence of a potential wash-off, where microgels  
736 saturated with okanin might have an advantage over buffer saturated with okanin.

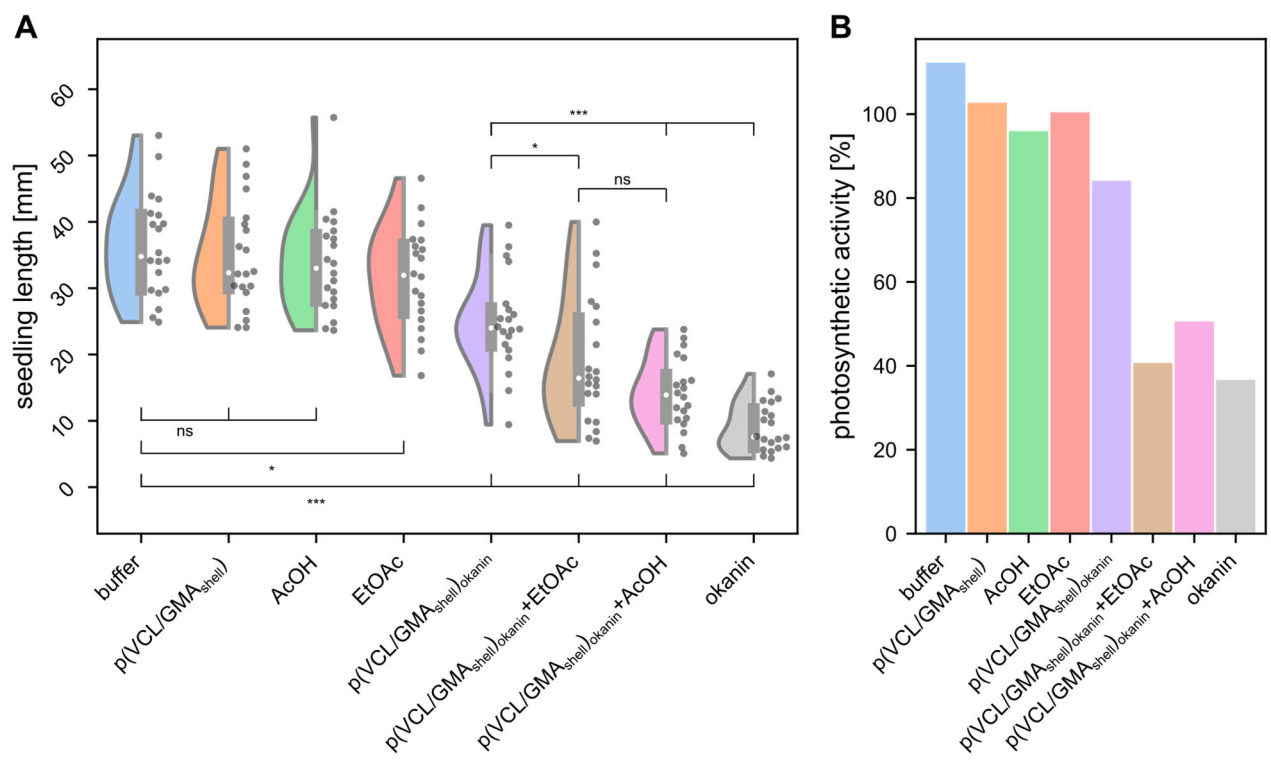


**Figure 8:** **A** Impact of organic solvents used for a triggered release, loaded and unloaded microgels, and combinations thereof on *A. retroflexus* seedling growth. Significance is evaluated using a two-sided Mann-Whitney U test; corresponding *p*-values are provided above/below the horizontal lines (ns: “not significant”, \*: *p* ≤ 0.05, \*\*\*: *p* ≤ 0.001; *n* = 20). The white dot displays the mean, the bars depict the quartiles. **B** Impact of organic solvents used for a triggered release, loaded and unloaded microgels, and combinations thereof on the relative photosynthetic activity of adult *A. retroflexus* plants. Photosynthetic activity before treatment was taken for reference (100%) (*n* = 1).

Likewise, on adult *A. retroflexus* plants, relative photosynthetic activity was determined for the above treatments (Figure 8B). The controls show minor differences to the activity before treatment (~100%). Okanin released from p(VCL/GMA<sub>shell</sub>) microgels yields an activity of ~80%. By contrast, solvent-triggered release of okanin from p(VCL/GMA<sub>shell</sub>) microgels results in a similar activity as okanin-saturated buffer, i.e., ~40 – 50% of remaining photosynthetic activity.

**Putative scope of the approach.** To evaluate if the pVCL-based microgels might be suitable for other established agrochemicals, we compared the shape and chemical features of okanin to 2634 known herbicides, fungicides, insecticides, or pesticides (see Supplemental Materials and Methods, Figure S44). The comparison of shape peaks around 0.75 (on a scale from 0 to 1 with 1 indicating perfect agreement), and the joint shape and chemical features comparison at 0.90 (on a scale from 0 to 2 with 2 indicating perfect agreement), indicating that, on average, the molecules are about half-way similar to okanin. We found several commercial herbicides, like Bromfenoxim, Aclonifen, Thifensulfuron-methyl, and Metsulfuron-methyl (Figure S45) that are similar to okanin, suggesting that pVCL-based microgels might also be a suitable carrier for them.

## 760 5 Conclusion

761 In this study, we investigated pVCL-based microgels as a potential carrier for okanin, an  
762 inhibitor of a C<sub>4</sub> plant key enzyme, in an integrated approach using experiments and simulations.  
763 The presented pVCL-based carriers should allow for tailoring the loading of okanin molecules,  
764 stabilization of okanin molecules in aqueous solution, and smart on-demand delivery of its cargo  
765 by exploiting release triggers such as treatment with aqueous co-solvents. DLS, AFM, and TEM  
766 analysis revealed that upon loading of okanin, pVCL microgels collapse and rigidify. The loading  
767 profile, i.e., the amount of loaded okanin with respect to the okanin concentration during loading,  
768 was determined using UV/Vis spectroscopy. By performing molecular dynamics simulations of  
769 oligomeric and crosslinked pVCL in combination with free energy calculations, we identified two  
770 different binding modes of okanin. Besides the adsorption of okanin to the pVCL chains, we found  
771 energetically favorable binding modes in which okanin mediates inter-chain crosslinks. For high  
772 okanin concentrations, we furthermore find stacking interactions of okanin not only within the  
773 solution but also with already adsorbed or bound okanin. Considering these states, the amount of  
774 bound okanin observed in simulations is in line with the experimentally determined loading  
775 profile. These findings can explain the experimentally observed collapse of the microgels and the  
776 rigidification of the particles. Decomposition of the binding free energy revealed polar interactions  
777 as a driving factor for okanin binding. Based on these results, we synthesized two p(VCL-co-  
778 GMA) microgels, where the GMA is localized within either the shell or core sections of the  
779 microgel. Independent of the GMA localization, the overall loading capacity of the microgels for  
780 okanin is doubled. Finally, we investigated the triggered release of okanin from the microgels by  
781 the addition of green solvents. Application of okanin-loaded p(VCL/GMA<sub>shell</sub>) microgels to  
782 seedlings and adult plants of *A. retroflexus* confirm the *in vitro* experiments and demonstrate a  
783 proof-of-principle for the application on plants.

784 Our findings show that p(VCL-co-GMA) microgels are promising potential carriers for the  
785 herbicide okanin. Next to the increased loading capacity of pVCL microgels that incorporate  
786 GMA, epoxy groups can be used for an easy surface modification of the microgel. If the epoxy  
787 groups are located within the shell of the microgel, they can be used to attach anchor peptides<sup>37</sup> to  
788 achieve an increased rain fastness of the carrier on the plant leaves. Finally, green solvents  
789 effectively triggered the (partial) release okanin, which provides a targeted way to release okanin  
790 on-demand. For the field application, this can potentially be achieved by a second spraying with  
791 an aqueous solution of a green solvent. Hence, this work establishes a basis for the further  
792 optimization of pVCL-based microgels for the delivery of herbicides with chemical properties  
793 such as okanin. In future works, the formulation efficiency in plant application has to be tested.

## 794 **6 Acknowledgements**

795 We gratefully acknowledge the computational support provided by the “Center for  
796 Information and Media Technology” (ZIM) at the Heinrich Heine University Düsseldorf and the  
797 computing time provided by the John von Neumann Institute for Computing (NIC) on the  
798 supercomputer JUWELS at Jülich Supercomputing Centre (JSC) (user IDs: HKF7, microgels).  
799 We are grateful to OpenEye for an academic license. We greatly acknowledge Hannah Mathews  
800 and Nadja Wolter, who performed STEM measurements as well as Marta Santi, who prepared  
801 samples for AFM and conducted the AFM measurements.

802

### 803 **ASSOCIATED CONTENT**

804 **Supporting Information.** This material is available free of charge via the internet at XXX.

805

### 806 **AUTHOR INFORMATION**

807 Corresponding Authors:

808 Andrij Pich

809 Address: Worringerweg 2, 52074 Aachen, Germany.

810 Phone: (+49) 241 80 23310

811 E-mail: pich@dwz.rwth-aachen.de

812 Holger Gohlke

813 Address: Universitätsstr. 1, 40225 Düsseldorf, Germany.

814 Phone: (+49) 211 81 13662; Fax: (+49) 211 81 13847

815 E-mail: gohlke@uni-duesseldorf.de

816

### 817 **Author Contributions**

818 J.D.<sup>†</sup> generated the atomistic models, performed the computational studies, analyzed results, and  
819 wrote the manuscript; F.K.<sup>†</sup> designed experiments, performed experimental studies, analyzed  
820 results, and wrote the manuscript; A.T. conceptualized experiments, analyzed results, and wrote  
821 the manuscript; A.H. designed, performed analyzed plant studies; G.G. contributed to conceiving  
822 the project, supervised and managed plant studies. A.P. conceived the study, supervised and  
823 managed the project, and wrote the manuscript; H.G. conceived the study, supervised and managed  
824 the project, and wrote the manuscript. All authors have approved the final version of the  
825 manuscript. <sup>†</sup>These authors contributed equally.

826

827 **FUNDING SOURCES**

828 This research is part of the scientific activities of the Bioeconomy Science Center, which were  
829 financially supported by the Ministry of Innovation, Science and Research of the German Federal  
830 State of North Rhine-Westphalia (MIWF) within the framework of the NRW Strategy Project  
831 BioSC (No. 313/323-400-00213) (funds to HG, AP, and GG within the FocusLab greenRelease).  
832 This work was performed in collaboration with the Center for Chemical Polymer Technology  
833 (CPT), which was supported by the EU (EUSMI, 731019) and the federal state of North Rhine-  
834 Westphalia (grant EFRE 300088302). We greatly acknowledge the Deutsche  
835 Forschungsgemeinschaft for financial support within the Collaborative Research Center SFB 985  
836 “Functional Microgels and Microgel Systems”.

837  
838 **NOTES**

839 The authors declare no competing financial interest.



## 840 7 References

- 841 1. Popp, J.; Pető, K.; Nagy, J., Pesticide productivity and food security. A review. *Agronomy for*  
842 *Sustainable Development* **2013**, *33* (1), 243-255.
- 843 2. Hunsche, M.; Alexeenko, A.; Damerow, L.; Noga, G., Rain-induced removal of copper from  
844 apple leaves: Influence of rain properties and tank-mix adjuvants on deposit characteristics at  
845 the micro scale. *Crop Protection* **2011**, *30* (4), 495-501.
- 846 3. Zhao, X.; Cui, H.; Wang, Y.; Sun, C.; Cui, B.; Zeng, Z., Development Strategies and Prospects  
847 of Nano-based Smart Pesticide Formulation. *Journal of Agricultural and Food Chemistry*  
848 **2018**, *66* (26), 6504-6512.
- 849 4. Roy, A.; Singh, S.; Bajpai, J.; Bajpai, A., Controlled pesticide release from biodegradable  
850 polymers. *Open Chemistry* **2014**, *12* (4), 453-469.
- 851 5. Athanassiou, C. G.; Kavallieratos, N. G.; Benelli, G.; Losic, D.; Usha Rani, P.; Desneux, N.,  
852 Nanoparticles for pest control: current status and future perspectives. *Journal of Pest Science*  
853 **2018**, *91* (1), 1-15.
- 854 6. Savary, S.; Willocquet, L.; Pethybridge, S. J.; Esker, P.; McRoberts, N.; Nelson, A., The  
855 global burden of pathogens and pests on major food crops. *Nature Ecology & Evolution* **2019**,  
856 *3* (3), 430-439.
- 857 7. Oerke, E. C., Crop losses to pests. *The Journal of Agricultural Science* **2006**, *144* (1), 31-43.
- 858 8. Nguyen, G. T. T.; Erlenkamp, G.; Jäck, O.; Küberl, A.; Bott, M.; Fiorani, F.; Gohlke, H.;  
859 Groth, G., Chalcone-based Selective Inhibitors of a C4 Plant Key Enzyme as Novel Potential  
860 Herbicides. *Sci. Rep.* **2016**, *6* (1), 27333.
- 861 9. Chotsaeng, N.; Laosinwattana, C.; Charoenying, P., Herbicidal Activity of Flavokawains and  
862 Related trans-Chalcones against *Amaranthus tricolor* L. and *Echinochloa crus-galli* (L.)  
863 Beauv. *ACS Omega* **2019**, *4* (24), 20748-20755.
- 864 10. Liu, X.; Chen, Y.; Deng, Y.; Xiao, C.; Luan, S.; Huang, Q., Novel Galactosyl Moiety-  
865 Conjugated Furylchalcones Synthesized Facilely Display Significant Regulatory Effect on  
866 Plant Growth. *Journal of Agricultural and Food Chemistry* **2022**, *70* (6), 1766-1775.
- 867 11. Minges, A.; Janßen, D.; Offermann, S.; Groth, G., Efficient In Vivo Screening Method for the  
868 Identification of C4 Photosynthesis Inhibitors Based on Cell Suspensions of the Single-Cell  
869 C4 Plant *Bienertia sinuspersici*. *Frontiers in Plant Science* **2019**, *10*.
- 870 12. Plamper, F. A.; Richtering, W., Functional Microgels and Microgel Systems. *Acc. Chem. Res.*  
871 **2017**, *50* (2), 131-140.
- 872 13. Karg, M.; Pich, A.; Hellweg, T.; Hoare, T.; Lyon, L. A.; Crassous, J. J.; Suzuki, D.; Gumerov,  
873 R. A.; Schneider, S.; Potemkin, I. I.; Richtering, W., Nanogels and Microgels: From Model  
874 Colloids to Applications, Recent Developments, and Future Trends. *Langmuir* **2019**, *35* (19),  
875 6231-6255.
- 876 14. Dirksen, M.; Dargel, C.; Meier, L.; Brändel, T.; Hellweg, T., Smart microgels as drug delivery  
877 vehicles for the natural drug aescin: uptake, release and interactions. *Colloid and Polymer*  
878 *Science* **2020**, *298* (6), 505-518.
- 879 15. Vihola, H.; Laukkanen, A.; Hirvonen, J.; Tenhu, H., Binding and release of drugs into and  
880 from thermosensitive poly(N-vinyl caprolactam) nanoparticles. *European Journal of*  
881 *Pharmaceutical Sciences* **2002**, *16* (1), 69-74.
- 882 16. Hoare, T.; Pelton, R., Impact of Microgel Morphology on Functionalized Microgel–Drug  
883 Interactions. *Langmuir* **2008**, *24* (3), 1005-1012.

- 884 17. Meurer, R. A.; Kemper, S.; Knopp, S.; Eichert, T.; Jakob, F.; Goldbach, H. E.; Schwaneberg,  
885 U.; Pich, A., Biofunctional Microgel-Based Fertilizers for Controlled Foliar Delivery of  
886 Nutrients to Plants. *Angew. Chem. Int. Ed.* **2017**, *56* (26), 7380-7386.
- 887 18. Wang, Y.; Nie, J.; Chang, B.; Sun, Y.; Yang, W., Poly(vinylcaprolactam)-Based  
888 Biodegradable Multiresponsive Microgels for Drug Delivery. *Biomacromolecules* **2013**, *14*  
889 (9), 3034-3046.
- 890 19. Li, X.; Li, H.; Zhang, C.; Pich, A.; Xing, L.; Shi, X., Intelligent nanogels with self-adaptive  
891 responsiveness for improved tumor drug delivery and augmented chemotherapy. *Bioactive*  
892 *Materials* **2021**, *6* (10), 3473-3484.
- 893 20. Li, X.; Sun, H.; Li, H.; Hu, C.; Luo, Y.; Shi, X.; Pich, A., Multi-Responsive Biodegradable  
894 Cationic Nanogels for Highly Efficient Treatment of Tumors. *Advanced Functional Materials*  
895 **2021**, *31* (26), 2100227.
- 896 21. Belthle, T.; Demco, D. E.; Pich, A., Nanostructuring the Interior of Stimuli-Responsive  
897 Microgels by N-Vinylimidazoles Quaternized with Hydrophobic Alkyl Chains.  
898 *Macromolecules* **2022**, *55* (3), 844-861.
- 899 22. Blackburn, W. H.; Dickerson, E. B.; Smith, M. H.; McDonald, J. F.; Lyon, L. A., Peptide-  
900 Functionalized Nanogels for Targeted siRNA Delivery. *Bioconjugate Chemistry* **2009**, *20* (5),  
901 960-968.
- 902 23. Malmsten, M.; Bysell, H.; Hansson, P., Biomacromolecules in microgels — Opportunities  
903 and challenges for drug delivery. *Current Opinion in Colloid & Interface Science* **2010**, *15*  
904 (6), 435-444.
- 905 24. Li, F.; Wang, C.; Guo, W., Multifunctional Poly-N-Isopropylacrylamide/DNAzyme  
906 Microgels as Highly Efficient and Recyclable Catalysts for Biosensing. *Advanced Functional*  
907 *Materials* **2018**, *28* (10), 1705876.
- 908 25. Steinhilber, D.; Rossow, T.; Wedepohl, S.; Paulus, F.; Seiffert, S.; Haag, R., A Microgel  
909 Construction Kit for Bioorthogonal Encapsulation and pH-Controlled Release of Living Cells.  
910 *Angewandte Chemie International Edition* **2013**, *52* (51), 13538-13543.
- 911 26. Vihola, H.; Laukkanen, A.; Valtola, L.; Tenhu, H.; Hirvonen, J., Cytotoxicity of  
912 thermosensitive polymers poly(N-isopropylacrylamide), poly(N-vinylcaprolactam) and  
913 amphiphilically modified poly(N-vinylcaprolactam). *Biomaterials* **2005**, *26* (16), 3055-3064.
- 914 27. Du, Y.; Lo, E.; Ali, S.; Khademhosseini, A., Directed assembly of cell-laden microgels for  
915 fabrication of 3D tissue constructs. *Proceedings of the National Academy of Sciences* **2008**,  
916 *105* (28), 9522-9527.
- 917 28. Ramos, J.; Imaz, A.; Forcada, J., Temperature-sensitive nanogels: poly(N-vinylcaprolactam)  
918 versus poly(N-isopropylacrylamide). *Polym. Chem.* **2012**, *3* (4), 852-856.
- 919 29. Schroeder, R.; Richtering, W.; Potemkin, I. I.; Pich, A., Stimuli-Responsive Zwitterionic  
920 Microgels with Covalent and Ionic Cross-Links. *Macromolecules* **2018**, *51* (17), 6707-6716.
- 921 30. López, C. M.; Pich, A., Supramolecular Stimuli-Responsive Microgels Crosslinked by Tannic  
922 Acid. *Macromolecular Rapid Communications* **2018**, *39* (6), 1700808.
- 923 31. Jung, S. H.; Bulut, S.; Busca Guerzoni, L. P. B.; Günther, D.; Braun, S.; De Laporte, L.; Pich,  
924 A., Fabrication of pH-degradable supramacromolecular microgels with tunable size and shape  
925 via droplet-based microfluidics. *Journal of Colloid and Interface Science* **2022**, *617*, 409-421.
- 926 32. Häntzschel, N.; Zhang, F.; Eckert, F.; Pich, A.; Winnik, M. A., Poly(N-vinylcaprolactam-co-  
927 glycidyl methacrylate) Aqueous Microgels Labeled with Fluorescent LaF3:Eu Nanoparticles.  
928 *Langmuir* **2007**, *23* (21), 10793-10800.

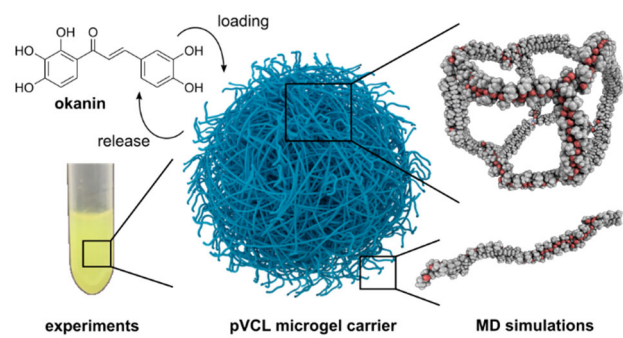
- 929 33. Häntzschel, N.; Hund, R.-D.; Hund, H.; Schrunner, M.; Lück, C.; Pich, A., Hybrid Microgels  
930 with Antibacterial Properties. *Macromol. Biosci.* **2009**, *9* (5), 444-449.
- 931 34. Gau, E.; Mate, D. M.; Zou, Z.; Oppermann, A.; Töpel, A.; Jakob, F.; Wöll, D.; Schwaneberg,  
932 U.; Pich, A., Sortase-Mediated Surface Functionalization of Stimuli-Responsive Microgels.  
933 *Biomacromolecules* **2017**, *18* (9), 2789-2798.
- 934 35. Singh, A.; Dhiman, N.; Kar, A. K.; Singh, D.; Purohit, M. P.; Ghosh, D.; Patnaik, S., Advances  
935 in controlled release pesticide formulations: Prospects to safer integrated pest management  
936 and sustainable agriculture. *Journal of Hazardous Materials* **2020**, *385*, 121525.
- 937 36. Trenkel, M. E., Slow- and Controlled-release and Stabilized Fertilizers: An Option for  
938 Enhancing Nutrient Use Efficiency in Agriculture. International Fertilizer Industry  
939 Association: 2010.
- 940 37. Dittrich, J.; Brethauer, C.; Goncharenko, L.; Bührmann, J.; Zeisler-Diehl, V.; Pariyar, S.;  
941 Jakob, F.; Kurkina, T.; Schreiber, L.; Schwaneberg, U.; Gohlke, H., Rational Design Yields  
942 Molecular Insights on Leaf-Binding of Anchor Peptides. *ACS Appl. Mater. Interfaces* **2022**.
- 943 38. Shahid, M. A.; Sarkhosh, A.; Khan, N.; Balal, R. M.; Ali, S.; Rossi, L.; Gómez, C.; Mattson,  
944 N.; Nasim, W.; Garcia-Sanchez, F., Insights into the Physiological and Biochemical Impacts  
945 of Salt Stress on Plant Growth and Development. *Agronomy* **2020**, *10* (7), 938.
- 946 39. Flowers, T. J.; Garcia, A.; Koyama, M.; Yeo, A. R., Breeding for salt tolerance in crop plants  
947 — the role of molecular biology. *Acta Physiologiae Plantarum* **1997**, *19* (4), 427-433.
- 948 40. Prat, D.; Wells, A.; Hayler, J.; Sneddon, H.; McElroy, C. R.; Abou-Shehata, S.; Dunn, P. J.,  
949 CHEM21 selection guide of classical- and less classical-solvents. *Green Chem.* **2016**, *18* (1),  
950 288-296.
- 951 41. Alfonsi, K.; Colberg, J.; Dunn, P. J.; Fevig, T.; Jennings, S.; Johnson, T. A.; Kleine, H. P.;  
952 Knight, C.; Nagy, M. A.; Perry, D. A.; Stefaniak, M., Green chemistry tools to influence a  
953 medicinal chemistry and research chemistry based organisation. *Green Chem.* **2008**, *10* (1),  
954 31-36.
- 955 42. Nečas, D.; Klapetek, P., Gwyddion: an open-source software for SPM data analysis. *Open*  
956 *Physics* **2012**, *10* (1), 181-188.
- 957 43. Rasband, W., ImageJ: Image processing and analysis in Java. *Astrophysics Source Code*  
958 *Library* **2012**, ascl: 1206.013.
- 959 44. Balaceanu, A.; Verkh, Y.; Kehren, D.; Tillmann, W.; Pich, A., Thermoresponsive Core-Shell  
960 Microgels. Synthesis and Characterisation. *Z. Phys. Chem.* **2014**, *228* (2-3), 253-267.
- 961 45. Jorgensen, W. L.; Chandrasekhar, J.; Madura, J. D.; Impey, R. W.; Klein, M. L., Comparison  
962 of simple potential functions for simulating liquid water. *J. Chem. Phys.* **1983**, *79* (2), 926-  
963 935.
- 964 46. Dittrich, J.; Kather, M.; Holzberger, A.; Pich, A.; Gohlke, H., Cumulative Submillisecond  
965 All-Atom Simulations of the Temperature-Induced Coil-to-Globule Transition of Poly(N-  
966 vinylcaprolactam) in Aqueous Solution. *Macromolecules* **2020**, *53* (22), 9793-9810.
- 967 47. Izadi, S.; Anandakrishnan, R.; Onufriev, A. V., Building Water Models: A Different  
968 Approach. *J. Phys. Chem. Lett.* **2014**, *5* (21), 3863-3871.
- 969 48. Bayly, C. I.; Cieplak, P.; Cornell, W.; Kollman, P. A., A well-behaved electrostatic potential  
970 based method using charge restraints for deriving atomic charges: the RESP model. *J. Phys.*  
971 *Chem.* **1993**, *97* (40), 10269-10280.

- 972 49. Frisch, M. J.; Trucks, G. W.; Schlegel, H. B.; Scuseria, G. E.; Robb, M. A.; Cheeseman, J. R.;  
973 Scalmani, G.; Barone, V.; Mennucci, B.; Petersson, G. A.; Nakatsuji, H.; Caricato, M.; Li, X.;  
974 Hratchian, H. P.; Izmaylov, A. F.; Bloino, J.; Zheng, G.; Sonnenberg, J. L.; Hada, M.; Ehara,  
975 M.; Toyota, K.; Fukuda, R.; Hasegawa, J.; Ishida, M.; Nakajima, T.; Honda, Y.; Kitao, O.;  
976 Nakai, H.; Vreven, T.; Montgomery, J. A., Jr.; Peralta, J. E.; Ogliaro, F.; Bearpark, M.; Heyd,  
977 J. J.; Brothers, E.; Kudin, K. N.; Staroverov, V. N.; Kobayashi, R.; Normand, J.;  
978 Raghavachari, K.; Rendell, A.; Burant, J. C.; Iyengar, S. S.; Tomasi, J.; Cossi, M.; Rega, N.;  
979 Millam, J. M.; Klene, M.; Knox, J. E.; Cross, J. B.; Bakken, V.; Adamo, C.; Jaramillo, J.;  
980 Gomperts, R.; Stratmann, R. E.; Yazyev, O.; Austin, A. J.; Cammi, R.; Pomelli, C.; Ochterski,  
981 J. W.; Martin, R. L.; Morokuma, K.; Zakrzewski, V. G.; Voth, G. A.; Salvador, P.;  
982 Dannenberg, J. J.; Dapprich, S.; Daniels, A. D.; Farkas, Ö.; Foresman, J. B.; Ortiz, J. V.;  
983 Cioslowski, J.; Fox, D. J. *Gaussian 09*, Revision A.02; Gaussian, Inc.: Wallingford CT, 2016.
- 984 50. Wang, J.; Wang, W.; Kollman, P. A.; Case, D. A., Automatic atom type and bond type  
985 perception in molecular mechanical calculations. *J. Mol. Graph. Model.* **2006**, 25 (2), 247-  
986 260.
- 987 51. Shelley, J. C.; Cholleti, A.; Frye, L. L.; Greenwood, J. R.; Timlin, M. R.; Uchimaya, M., Epik:  
988 a software program for pK( a ) prediction and protonation state generation for drug-like  
989 molecules. *J. Comput. Aided Mol. Des.* **2007**, 21 (12), 681-91.
- 990 52. Schrödinger *Maestro*, Schrödinger: New York, NY, 2019.
- 991 53. Case, D. A.; Ben-Shalom, I. Y.; Brozell, S. R.; Cerutti, D. S.; Cheatham III, T. E.; Cruzeiro,  
992 V. W. D.; Darden, T. A.; Duke, R. E.; Ghoreishi, D.; Gilson, M. K.; Gohlke, H.; Goetz, A.  
993 W.; Greene, D.; Harris, R.; Homeyer, N.; Izadi, S.; Kovalenko, A.; Kurtzman, T.; Lee, T. S.;  
994 LeGrand, S.; Li, P.; Lin, C.; Liu, J.; Luchko, T.; Luo, R.; Mermelstein, D. J.; Merz, K. M.;  
995 Miao, Y.; Monard, G.; Nguyen, C.; Nguyen, H.; Omelyan, I.; Onufriev, A.; Pan, F.; Qi, R.;  
996 Roe, D. R.; Roitberg, A.; Sagui, C.; Schott-Verdugo, S.; Shen, J.; Simmerling, C. L.; Smith,  
997 J.; Salomon-Ferrer, R.; Swails, J.; Walker, R. C.; Wang, J.; Wei, H.; Wolf, R. M.; Wu, X.;  
998 Xiao, L.; York, D. M.; Kollman, P. A. *AMBER*, University of California: San Francisco,  
999 2021.
- 1000 54. Case, D. A.; Cheatham III, T. E.; Darden, T.; Gohlke, H.; Luo, R.; Merz Jr., K. M.; Onufriev,  
1001 A.; Simmerling, C.; Wang, B.; Woods, R. J., The Amber biomolecular simulation programs.  
1002 *J. Comput. Chem.* **2005**, 26 (16), 1668-1688.
- 1003 55. Salomon-Ferrer, R.; Götz, A. W.; Poole, D.; Le Grand, S.; Walker, R. C., Routine  
1004 Microsecond Molecular Dynamics Simulations with AMBER on GPUs. 2. Explicit Solvent  
1005 Particle Mesh Ewald. *J. Chem. Theory Comput.* **2013**, 9 (9), 3878-3888.
- 1006 56. Le Grand, S.; Götz, A. W.; Walker, R. C., SPFP: Speed without compromise—A mixed  
1007 precision model for GPU accelerated molecular dynamics simulations. *Comput. Phys.*  
1008 *Commun.* **2013**, 184 (2), 374-380.
- 1009 57. Wang, J.; Wolf, R. M.; Caldwell, J. W.; Kollman, P. A.; Case, D. A., Development and testing  
1010 of a general amber force field. *J. Comput. Chem.* **2004**, 25 (9), 1157-1174.
- 1011 58. Martínez, L.; Andrade, R.; Birgin, E. G.; Martínez, J. M., PACKMOL: A package for building  
1012 initial configurations for molecular dynamics simulations. *J. Comput. Chem.* **2009**, 30 (13),  
1013 2157-2164.
- 1014 59. Darden, T.; York, D.; Pedersen, L., Particle mesh Ewald: An N·log(N) method for Ewald  
1015 sums in large systems. *J. Chem. Phys.* **1993**, 98 (12), 10089-10092.

- 1016 60. Ryckaert, J.-P.; Ciccotti, G.; Berendsen, H. J. C., Numerical integration of the cartesian  
1017 equations of motion of a system with constraints: molecular dynamics of n-alkanes. *J.*  
1018 *Comput. Phys.* **1977**, *23* (3), 327-341.
- 1019 61. Nguyen, H.; Roe, D. R.; Swails, J.; Case, D. A. PYTRAJ: Interactive data analysis for  
1020 molecular dynamics simulations. , 2016.
- 1021 62. Roe, D. R.; Cheatham, T. E., PTRAJ and CPPTRAJ: Software for Processing and Analysis of  
1022 Molecular Dynamics Trajectory Data. *J. Chem. Theory Comput.* **2013**, *9* (7), 3084-3095.
- 1023 63. Srinivasan, J.; Cheatham, T. E.; Cieplak, P.; Kollman, P. A.; Case, D. A., Continuum Solvent  
1024 Studies of the Stability of DNA, RNA, and Phosphoramidate–DNA Helices. *J. Am. Chem.*  
1025 *Soc.* **1998**, *120* (37), 9401-9409.
- 1026 64. Kollman, P. A.; Massova, I.; Reyes, C.; Kuhn, B.; Huo, S.; Chong, L.; Lee, M.; Lee, T.; Duan,  
1027 Y.; Wang, W.; Donini, O.; Cieplak, P.; Srinivasan, J.; Case, D. A.; Cheatham, T. E.,  
1028 Calculating Structures and Free Energies of Complex Molecules: Combining Molecular  
1029 Mechanics and Continuum Models. *Acc. Chem. Res.* **2000**, *33* (12), 889-897.
- 1030 65. Massova, I.; Kollman, P. A., Combined molecular mechanical and continuum solvent  
1031 approach (MM-PBSA/GBSA) to predict ligand binding. *Perspect. Drug Discov. Des.* **2000**,  
1032 *18* (1), 113-135.
- 1033 66. Homeyer, N.; Gohlke, H., Free Energy Calculations by the Molecular Mechanics  
1034 Poisson–Boltzmann Surface Area Method. *Mol. Inform.* **2012**, *31* (2), 114-122.
- 1035 67. Case, D. A., Normal mode analysis of protein dynamics. *Curr. Opin. Struct. Biol.* **1994**, *4* (2),  
1036 285-290.
- 1037 68. Miller, B. R.; McGee, T. D.; Swails, J. M.; Homeyer, N.; Gohlke, H.; Roitberg, A. E.,  
1038 MMPBSA.py: An Efficient Program for End-State Free Energy Calculations. *J. Chem. Theory*  
1039 *Comput.* **2012**, *8* (9), 3314-3321.
- 1040 69. Honig, B.; Nicholls, A., Classical electrostatics in biology and chemistry. *Science* **1995**, *268*  
1041 (5214), 1144-1149.
- 1042 70. Gilson, M. K.; Sharp, K. A.; Honig, B. H., Calculating the electrostatic potential of molecules  
1043 in solution: Method and error assessment. *J. Comput. Chem.* **1988**, *9* (4), 327-335.
- 1044 71. Tan, C.; Tan, Y.-H.; Luo, R., Implicit Nonpolar Solvent Models. *J. Phys. Chem. B* **2007**, *111*  
1045 (42), 12263-12274.
- 1046 72. McQuarrie, D. A., *Statistical Mechanics*. 2nd ed.; University Science Books: 2000.
- 1047 73. Hawkins, G. D.; Cramer, C. J.; Truhlar, D. G., Pairwise solute descreening of solute charges  
1048 from a dielectric medium. *Chem. Phys. Lett.* **1995**, *246* (1), 122-129.
- 1049 74. Hawkins, G. D.; Cramer, C. J.; Truhlar, D. G., Parametrized Models of Aqueous Free Energies  
1050 of Solvation Based on Pairwise Descreening of Solute Atomic Charges from a Dielectric  
1051 Medium. *J. Phys. Chem.* **1996**, *100* (51), 19824-19839.
- 1052 75. Janin, J., For Guldberg and Waage, with love and cratic entropy. *Proteins: Structure,*  
1053 *Function, and Bioinformatics* **1996**, *24* (4), i-ii.
- 1054 76. Gilson, M. K.; Given, J. A.; Bush, B. L.; McCammon, J. A., The statistical-thermodynamic  
1055 basis for computation of binding affinities: a critical review. *Biophys. J.* **1997**, *72* (3), 1047-  
1056 1069.
- 1057 77. Luo, H.; Sharp, K., On the calculation of absolute macromolecular binding free energies.  
1058 *PNAS* **2002**, *99* (16), 10399-10404.

- 1059 78. Narang, P.; de Oliveira, T. E.; Venkatesu, P.; Netz, P. A., The role of osmolytes in the  
1060 temperature-triggered conformational transition of poly(N-vinylcaprolactam): an  
1061 experimental and computational study. *Phys. Chem. Chem. Phys.* **2020**, 22 (9), 5301-5313.
- 1062 79. Umapathi, R.; Venkatesu, P., Assessing the efficiency of imidazolium-based ionic liquids on  
1063 the phase behavior of a synthetic biomedical thermoresponsive polymer. *J. Colloid Interface*  
1064 *Sci.* **2018**, 511, 174-183.
- 1065 80. Fan, H.; Wang, L.; Feng, X.; Bu, Y.; Wu, D.; Jin, Z., Supramolecular Hydrogel Formation  
1066 Based on Tannic Acid. *Macromolecules* **2017**, 50 (2), 666-676.
- 1067

1068 **8 TOC Figure**



1069  
1070 For Table of Contents only.